ROBUST CONTROLLER DESIGN FOR A FIXED-WING UAV USING ACTIVE DISTURBANCE CANCELLATION

by
Nadeen Hashem

Submitted to
the Graduate School of Engineering and Natural Sciences
in partial fulfillment of
the requirements for the degree of
Master of Science

Sabanci University
December, 2023

ROBUST CONTROLLER DESIGN FOR A FIXED-WING UAV
USING ACTIVE DISTURBANCE CANCELLATION

Nadeen Hashem

APPROVED BY

Prof. Dr. Mustafa Ünel ..... (Thesis Advisor)

Assoc. Prof. Dr. Kemalettin Erbatur .....

Assoc. Prof. Dr. Hüseyin Üvet .....

DATE OF APPROVAL: .....

ABSTRACT

ROBUST CONTROLLER DESIGN FOR A FIXED-WING UAV
USING ACTIVE DISTURBANCE CANCELLATION

NADEEN HASHEM

ME, Master's Thesis, December 2023

Thesis Advisor: Prof. Dr. Mustafa Ünel

Keywords: Fixed-Wing UAV, Gain Scheduling, PID Control, Disturbance Observer, Conditional Integral Sliding Mode Control

Autonomous aerial vehicles have become integral components of both military and civilian applications, playing crucial roles in tasks such as reconnaissance, surveillance, and inspection. Given their widespread use, extensive research contributions aim to further enhance their performance. Among the key areas of investigation for autonomous aerial vehicles, research into control system architectures used in the autopilots stands out as particularly significant. The main aim of ongoing research is to find control architectures that are not only robust but also fulfill other criteria such as being easy to implement and cost-effective, making them practical for real-world applications.

This thesis focuses on the robust controller design of a fixed-wing UAV through the application of active disturbance cancellation methods in addressing the longitudinal instability of a fixed-wing UAV's aerodynamics. Pitch stabilization is achieved through the utilization of a gain-scheduled controller based on Proportional-Integral-Derivative (PID) control. To evaluate the robustness of the gain-scheduled controller, simulations are conducted across three distinct flight stages representing different trim points of the UAV: steady-level flight at sea level, pull-up flight, and steady-level flight at a certain altitude. These simulations are carried out separately, introducing fixed disturbance and disturbance produced by the Dryden

wind model. Following this, a disturbance observer is integrated into the gain-scheduled controller to further enhance its robustness. Subsequently, a Conditional Integral Sliding Mode Controller (C-ISMC) is designed and tested for both nominal and fixed disturbance scenarios, with a comparative analysis against the gain-scheduled controller. This was followed by the integration of a disturbance observer into the C-ISMC to evaluate its robustness against wind disturbance. Results obtained from the C-ISMC with a disturbance observer exhibits higher robustness than the disturbance observer based gain-scheduled controller.

ÖZET

Aktif Bozucu İptali Kullanarak Sabit Kanatlı Bir İHA İçin Dayanıklı Kontrolör Tasarımı

NADEEN HASHEM

ME, Master Tezi, Aralık 2023

Tez Danışmanı: Prof. Dr. Mustafa Ünel

Anahtar kelimeler: Sabit Kanatlı İHA, Kazanç Programlaması, PID Kontrol, Bozucu Gözlemci, Koşullu Integral Kayan Kipli Kontrol

Otonom hava araçları, hem askeri hem de sivil uygulamalarda temel bileşenler haline gelmiş olup, keşif, gözetleme ve denetleme gibi görevlerde kritik roller oynamaktadır. Geniş bir kullanım alanına sahip olmaları nedeniyle, performanslarını daha da geliştirmeye yönelik geniş çaplı araştırma katkıları bulunmaktadır. Özerk hava araçlarıyla ilgili ana araştırma alanları arasında, otomatik pilotlarda kullanılan kontrol sistem mimarilerine yönelik araştırmalar özellikle önemlidir. Devam eden araştırmanın temel amacı, sadece dayanıklı değil aynı zamanda uygulamasının kolay ve maliyet etkili olacak şekilde diğer kriterleri de karşılayan kontrol mimarileri bulmaktır, bu da onları gerçek dünya uygulamaları için pratik hale getirir.

Bu tez, sabit kanatlı bir İnsansız Hava Aracı (İHA) için dayanıklı bir denetleyici tasarımına odaklanarak, aktif bozucu iptal yöntemlerinin uygulanması yoluyla sabit kanatlı bir İHA'nın aerodinamiğindeki uzunlamasına kararsızlığı ele almaktadır. Yunuslama stabilizasyonu, Oransal-Integral-Türevsel (PID) kontrole dayalı bir kazanç programlamalı denetleyici kullanılarak elde edilmektedir. Kazanç programlamalı denetleyicinin dayanıklılığını değerlendirmek amacıyla, İHA'nın farklı trim noktalarını temsil eden üç ayrı uçuş aşamasında simulasyonlar gerçekleştirilmiştir: deniz seviyesinde düz seviyede uçuş, çıkış uçuşu ve belirli bir yükseklikte düz seviyede uçuş. Bu simulasyonlar ayrı ayrı gerçekleştirilirken sabit bozucu ve Dryden rüzgar modeli tarafından üretilen bozucu kullanılmıştır. Bundan sonra, bir bozucu gözlemci, kazanç

programlamalı denetleyiciye daha fazla dayanıklılık kazandırmak amacıyla bu denetleyiciye entegre edilmiştir. Daha sonra, nominal ve sabit bozucu senaryoları için Koşullu Integral Kayan Kipli Denetleyici (C-ISMC) tasarlanmış ve test edilmiştir ve kazanç programlamalı denetleyici ile karşılaştırmalı bir analiz yapılmıştır. Bunun ardından, bir bozucu gözlemci C-ISMC'ye entegre edilerek, rüzgar bozucusuna karşı dayanıklılığı değerlendirilmiş-tir. C-ISMC'den elde edilen sonuçlar, bozucu gözlemci temelli kazanç programlamalı denetleyici-den daha yüksek dayanıklılık sergilemektedir.

ACKNOWLEDGEMENTS

I wish to extend my appreciation to my advisor, Prof. Dr. Müstafa Ünel, for his invaluable support throughout the completion of my thesis. His guidance and assistance were essential to achieve this work. I have learnt a lot from him, not only as a graduate student, but also as an undergraduate student. I feel lucky to have worked with him on my Master's Thesis; he is truly one of the most exceptional and dedicated professors I have encountered.

I wish to express my gratitude to Assoc. Prof. Dr. Kemalettin Erbatur and Assoc. Prof. Hüseyin Üvet for their meticulous review of my thesis and for offering constructive comments and valuable suggestions.

I also want to convey sincere thanks to my friend Burak Er, who consistently offered assistance and support whenever it was needed.

Finally, my profound love and gratitude go to my family, who have been unwavering in their support and encouragement throughout my entire life, shaping me into the person I am today.

TABLE OF COTENTS

LIST OF FIGURES

LIST OF TABLES

LIST OF SYMBOLS

α	Angle of Attack
β	Sideslip Angle
S	Wing Area
$\bar{c}$	Wing Chord
b	Wing Span
$C_{X,t}$	Total X-axis force coefficient
$C_{Y,t}$	Total Y-axis force coefficient
$C_{Z,t}$	Total Z-axis force coefficient
$C_{l,t}$	Total rolling moment coefficient
$C_{l,t}$	Total pitching moment coefficient
$C_{l,t}$	Total yawing moment coefficient
I_{xx}	Moment of inertia about X-axis
I_{yy}	Moment of inertia about Y-axis
I_{zz}	Moment of inertia about Z-axis
m	Mass of aircraft
X_A	Total X-axis aerodynamic force
Y_A	Total Y-axis aerodynamic force
Z_A	Total Z-axis aerodynamic force
T	Thrust
p	Roll angular rate
q	Pitch angular rate
r	Yaw angular rate
u	Linear velocity in X-axis
v	Linear velocity in Y-axis

w	Linear velocity in Z-axis
δe	Elevator deflection
δa	Aileron deflection
δr	Rudder deflection
ϕ	Roll angle
θ	Pitch angle
ψ	Yaw angle
H_e	Angular momentum of engine
V	True Airspeed

CHAPTER 1

INTRODUCTION

The advancement of affordable wireless communication, GPS, on-board cameras, inertial measurement unit (IMU) sensor suites, and data processing techniques has resulted in the widespread availability of unmanned aerial vehicles (UAVs) equipped with onboard autopilot systems [1, 2].In the present day, Unmanned Aerial Vehicles (UAVs) represent a thriving sector in aerospace industry. They are proving to be immensely beneficial today, not only in military applications but also in civilian use. This is attributed to their numerous advantages when compared to manned aerial vehicles. Given their smaller size compared to manned aircrafts [3], UAVs generally involve lower manufacturing and operational costs.Moreover,they contribute to the preservation of human lives by eliminating the need for human involvement in hazardous and challenging missions, and, without a flight crew, they can achieve higher velocities and undertake riskier maneuvers.

Some of the military applications of UAVs encompass reconnaissance, surveillance, and target acquisition (RSTA), peacetime and combat Synthetic Aperture Radar (SAR) surveillance [4, 5, 6, 7], deception operations, maritime operations such as naval fire support and ship classification, applications involving Unmanned Combat Air Vehicles (UCAVs), meteorology missions [8], route and landing reconnaissance support, electronic warfare (EW), and Signals Intelligence (SIGINT), as well as radio and data relay. Additionally, in civil applications [9], UAVs play a role in search and rescue efforts[10, 11], locating missing individuals

in remote or challenging areas and monitoring large-scale emergencies. In agriculture, they are utilized for tasks such as seed planting, weed identification, and crop forecasting [12, 13, 14]. Furthermore, UAVs are employed for goods delivery [15] and in infrastructure development, where they contribute to monitoring the structural health of bridges and dams [16, 17]. Figure 1.1 shows three applications of UAVs. Subfigures 1.1(a) and 1.1(b) show the X-45 Unmanned Combat Air Vehicle (UCAV) [18] and MQ-1 Predator UAV [19] , respectively, both designed for use in combat and military operations. Meanwhile, Subfigure 1.1(c) depicts a UAV specifically utilized for agricultural surveying purposes [20] .

(a) X-45 UCAV

(b) MQ-1 Predator UAV

(c) UX11 Agricultural UAV

Figure 1.1: Different UAV Applications

1.1 Motivation

With the rapid progress of technology, UAVs are increasingly becoming an indispensable part of our lives. The significance attached to these devices requires ongoing research to continually enhance their autopilot systems. The autopilot, a device integrated into UAVs, facilitates the control of the aircraft without direct human intervention (see Figure 1.2) [21]. These systems consist of a combination of sensors, actuators, and algorithms to interpret data related to the vehicle's position, orientation, and external conditions. This enables them to take actions, ensuring the UAV maintains its intended trajectory or executes a desired maneuvers. Examples of utilized autopilot systems for UAVs include PixHawk and DJI Naza.

Figure 1.2: Pixhawk autopilot

A common focus in UAV research lies in the exploration of control systems for autopilots. These systems are crucial for regulating the aircraft's behavior, ensuring stability, and attaining desired performance. Consequently, extensive research endeavors continuously introduce different robust control algorithms to contribute to the advancement of the autopilot control systems.

In response to this challenge, ongoing research explores more robust alternatives. While these controllers often offer superior performance compared to PID controllers, their implementation tends to be more complex and costly. Therefore, despite the advancements in UAV control design research, PID remains the primary choice, given its balance of simplicity, cost-effectiveness, and satisfactory performance.

1.2 Contributions of the Thesis

The contributions of the thesis can be summarized as follows:

- Development of a mathematical model for a fixed-wing UAV.
- Designing and tuning a gain-scheduled controller.
- Designing a Disturbance Observer-Based Controller which consists of a gain-scheduled PID controller and linear disturbance observer.
- Designing a second Disturbance Observer-Based Controller which consists of a Conditional Integral Sliding Mode Controller (C-ISMC) and linear disturbance observer.

- Simulation results to compare between the robustness of the controllers.

1.3 Outline of the Thesis

The thesis is organized as follows: Chapter 2 provides a comprehensive literature review on fixed-wing UAVs and controllers. Chapter 3 delves into the modeling of the fixed-wing aircraft, offering detailed insights into the implementation of the 6 DOF equations of motion, aerodynamic model, atmospheric model, and engine model. Additionally, it illustrates the main reference frames and coordinate systems. Chapter 4 covers the application of controllers, which are PID based gain scheduling controllers with and without disturbance observer, commonly referred to as the disturbance observer-based controller (DOBC).In addition, a conditional integral sliding mode controller has also been designed and implemented with and without disturbance observer. Chapter 5 thoroughly interprets the simulation results. Chapter 6 offers a conclusion summarizing key findings and provides recommendations for future research endeavors.

1.4 Publications

In preparation

CHAPTER 2

LITERATURE SURVEY AND BACKGROUND

This chapter offers an overview of unmanned aerial vehicles and explores a range of control systems that are used in the autopilots. Additionally, it explores the research efforts aimed at improving the design of controls for UAVs.

2.1 Unmanned Aerial Vehicles

An Unmanned Aerial Vehicle (UAV) is an aircraft that functions without a human pilot onboard, operating either autonomously or under the remote control of a pilot in a ground station. Initially designed primarily for military purposes due to their high costs, UAVs have witnessed a reduction in expenses over time. This cost decline is attributed to advancements in technology across various domains, including electronics, materials science, and control systems. As a result, the decreased costs have facilitated increased production and the widespread adoption of UAVs in civil applications. In military applicationss, UAVs are used in tasks such as reconnaissance, surveillance, and target acquisition. In civil applica-

tions, UAVs are utilized for purposes such as search and rescue operations, infrastructure inspection, and agricultural activities.

UAVs attain their autonomy or semi-autonomy through the use of autopilots. Autopilots comprise a combination of sensors including GPS, Inertial Measurement Units (IMUs), magnetometers, and barometers. Additionally, they include processors and control algorithms that issue commands to the aircraft to achieve the desired flight performance.

Unmanned Aerial Vehicles (UAVs) can be classified into three distinct types: Multirotor UAVs, fixed-wing UAVs, and hybrid UAVs. Each configuration possesses unique characteristics, serving specific operational needs.

Multirotor UAVs, characterized by their ability to take off and land vertically and thus eliminating the need for a runway or catapult, makes them the best option for scenarios for operations within confined spaces. Their exceptional maneuverability and swift directional changes make them ideal for tasks demanding close proximity to objects or agile flight.

On the other hand, fixed-wing UAVs are recognized for their extended flight endurance and superior range. The aerodynamic design of these UAVs enables them to cover vast distances efficiently, making them energy-efficient for long flights. With the capacity to carry larger payloads compared to multirotors, fixed-wing UAVs find applications in tasks demanding the use of heavier sensors or equipment. Moreover, their operational advantages extend to higher altitudes, making them well-suited for tasks like aerial mapping and surveillance, where a broader perspective is crucial.

Hybrid UAVs represent a convergence of features from both fixed-wing and multirotor configurations. By combining the vertical takeoff and landing capabilities of multirotors with the efficiency and endurance of fixed-wing aircraft, hybrids aim to harness the strengths of both configurations. This versatility allows for adaptability to diverse mission profiles, offering advantages in scenarios where a combination of hovering and long-range flight is essential.

In summary, the differences among multirotor, fixed-wing, and hybrid UAVs involve factors such as maneuverability, endurance, range, payload capacity, and operational versatility. Figure 2.1 presents the three different configurations [22, 23, 24]

(a) Fixed-wing UAV (b) Multirotor UAV (c) Hybrid UAV

Figure 2.1: Different UAV Applications

2.2 Control Systems

Due to their superior endurance and energy efficiency when compared to multirotor UAVs, fixed wing UAVs are commonly used in large area surveillance, mapping, search and rescue in remote areas, military surveillance and reconnaissance, and meteorological research. The ongoing pursuit of improving the overall performance of fixed-wing UAVs for these applications drives persistent research endeavors. Among the fundamental research areas, a significant focus lies on developing more robust control designs that can effectively achieve the desired performance for these unmanned aerial vehicles.

2.2.1 Linear Controllers

To meet the simplicity requirement for UAV controller design, numerous research studies have concentrated on developing linear controllers like PID, LQR, and LPV. The LQR controller design is based on linearized models of UAV dynamics and uses quadratic cost functions to enhance control performance. Because of its simplicity and effectiveness in managing linear systems, LQR controller is widely used for achieving stable and optimal control. For instance, Dharmawan et al. [25] utilized the LQR controller to create an obstacle avoidance system. In another study [26], LQR was used to control the longitudinal dynamics of an aircraft in order to attenuate the effcts of microburst encounters. It is important to acknowledge that as the LQR is designed based on a linearized model, its optimal performance is observed in the vicinity of the system's linearized point. Consequently, for UAVs operating at different

operational conditions, more adaptive and robust controllers should be used.

It is noteworthy that the PID (Proportional-Integral-Derivative) controller emerges as the most widely implemented controller for UAVs. This prevalence is attributed to its simplicity, cost-effectiveness in comparison to other controllers, and its capability to deliver satisfactory performance. In their work, Poksawat et al. [27] introduced an automatic tuning method for a PID controller based on relay feedback control. However,it was observed that the results had significant oscillatory behavior since the tuned coefficients were not applicable under different operational conditions. Consequently, the authors published a subsequent paper [28], where they propose the automatic tuning of a gain-scheduled PID controller using a relay feedback test. Through wind tunnel experiments conducted under relay feedback control, the parameters of the PI controller were determined. The proposed controller demonstrated a reduced attitude deviation from the reference compared to the PID controller.

Another type of linear controller is the LPV (Linear Parameter-Varying) controller. Unlike PID and LQR, the LPV controller parameters vary dynamically according to the system's operational conditions. LPV controllers are a type of adaptive control that provide a continuous, smooth transition between different linear models based on the varying parameters. In [29], several path-following controllers are designed for a small fixed-wing unmanned aircraft system (UAS). Among these controllers is a linear parameter-varying (LPV) controller, which is scheduled based on path curvature.

2.2.2 Non-Linear Controllers

While linear controllers, such as PID and LQR controllers, meet the simplicity requirements of UAV controllers, they exhibit sensitivity to external disturbances, sensor noise, and are not applicable across various flight stages. In response to these challenges, researchers propose more robust non-linear controllers in the pursuit of enhancing flight performance.

One of the most famous non-linear controllers used is the Non-linear Dynamic Inversion controller (NDI). The basic idea behind dynamic inversion is to first invert or linearize the dynamic model of the system and then design a controller for the inverted or linearized model. This approach is particularly useful for systems with nonlinear dynamics. Wacker et. al. [30] proposed a control system which combines a nonlinear Dynamic Inversion controller

for rate compensation and a classic Proportional-Integral (PI) controller for tracking attitude angle commands. Flight tests prove that proposed controller the was able to meet the robust stability requirements. In another study [31],an Incremental Nonlinear Dynamic Inversion (INDI) combined with a neural network adaptive controller to obtain high angle maneuvers is proposed. Simulations prove that the proposed controller achieves robustness and good tracking performance.

Another common non-linear controller is the sliding mode controller (SMC). The key idea of SMC is to design a function in terms of the system's error called the sliding variable, with the objective of driving it to zero. After the variable reaches zero , a properly designed sliding surface is introduced in which the system's trajectory is compelled to follow [32]. In one study, Bao et. al. [33] combined a backstepping sliding mode controller with an adaptive law to estimate parameter uncertainties in the model and external disturbances and consequently compensate for them. It is demonstrated that the tracking error converges to zero and that the controller exhibits the capability to effectively and stably control a fixed-wing UAV, successfully overcoming disturbances and uncertainties. In the study by Espinoza et al. [34] five different controllers are used; backstepping control, the sliding mode control, backstepping with sliding mode control, backstepping with two sliding mode control, and backstepping with high order sliding mode. The simulation results prove that the backstepping with high order sliding mode obtains the best robustness and least chattering.

Model Predictive Controller is another type of controller commonly used in various industries. It is based on the model of the system dynamics which predicts the future behavior of the system based on the control inputs and the system's current state. Mathisen et. al. [35] propose an on-line non-linear model predictive controller (NMPC) in order to obtain a guided deep-stall for landing purposes. Results show that the proposed controller achieves deep-stall landing with good precision. In [36] an NMPC obtained good convergence results for trajectory tracking of a fixed-wing UAV.

2.2.3 Gain Scheduling

Gain scheduling is a control strategy that is considered to be a compromise between fixed and adaptive control. Fixed control examples are LQR and PID, where a set of defined parameters

of the controller are used for the system and are fixed through all the various operating points of the system.To overcome this limitation without resorting to nonlinear adaptive controllers, gain scheduling emerges as a viable solution. Gain scheduling dynamically adjusts the parameters of a controller based on changes in the operating conditions of the system being controlled.

Poksawat et. al. [28] applied the automatic tuning algorithm to a gain-scheduled PID controller after they saw the suboptimal performance of their fixed-parameter PID controller without gain scheduling. The proposed controller demonstrated a reduced attitude deviation from the reference compared to the PID controller. In [37] a gain-scheduled H_∞ controller is proposed resulting in superior performance compared to the application of the H_∞ controller alone. Silva et. al. [38] propose using dynamic inversion control and a gain scheduled P controller for a tailsitter UAV. The proposed controller demonstrates better performance in comparison to a PI controller.

2.2.4 Disturbance Observer

Disturbances and uncertainties are widespread in various industrial systems, negatively impacting the stability and performance of control systems. [39, 40, 41]. As a result, disturbance rejection is one of the most important objectives in control system design. While measuring disturbances and subsequently canceling them through feedback systems is a viable approach, practical challenges often arise due to the non-measurability or high cost of disturbances. In response to this, estimating disturbance is considered one of the most practical ways in order to reject disturbances in control systems [42].

Disturbance observers present an effective technique for estimating disturbances. Their operation involves comparing the system's actual outputs with the expected outputs and attributing any differences to disturbances. This process facilitates disturbance cancellation, making disturbance observers valuable components for controllers. Through disturbance attenuation, they significantly enhance the robustness of the control system. Disturbance observers can be integrated to various types of controllers, such as PID [43], Sliding mode controller[44], MPC [45], and Feedback Linearization [46].

Some of the reserach about disturbance observer applications to fixed wing UAV con-

trol systems include the following studies. In [47], a novel coordinated disturbance observer (CDOB) which consists of multiple disturbance observers integrated. This innovative approach demonstrates its effectiveness in canceling disturbances and enhancing the robustness of the system. Smith et. al. [48] applied a disturbance observer control based on Linear Quadratic Regulator with Integral Action (LQI). Through gust alleviation, the proposed method has demonstrated enhanced stability and improved performance compared to using LQI alone. Yang et. al. [49] introduce an optimal offset-free path-following algorithm designed for fixed-wing UAVs. A nonlinear disturbance observer is integrated to the algorithm in order to estimate and compensate for wind effects. Simulation results prove the viability and efficiency of the proposed approach.

CHAPTER 3

AIRCRAFT MODELING

To assess controllers before their implementation on UAVs, it is essential to initially construct a mathematical model of the vehicle. This model serves as the basis for testing and fine-tuning controller parameters. Consequently, this chapter offers a comprehensive explanation of the fixed-wing aircraft's modeling, providing a thorough understanding of both its kinematics and dynamics.

3.1 Model Description

The aircraft exhibits three primary motions: roll, pitch, and yaw. Roll involves a moment around the body x-axis, pitch entails a moment around the body y-axis, and yaw comprises a moment around the body z-axis, as illustrated in Figure 3.1.

The system has four inputs, three of them from the actuators ($\delta a, \delta e, \delta r$) —namely, the ailerons, elevators, and rudders—while the fourth input is provided by the pilot, which is throttle (δt). There is a pair of aileron control surfaces, one on each wing, facilitating the roll motion by moving simultaneously in opposite directions. This action alters lift distribution, increasing lift on one wing while decreasing it on the other. The elevator control surface,

situated on the horizontal tail, governs pitch motion. The rudder control surface, positioned on the vertical tail, is responsible for yaw motion. It's worth noting that the specific locations of control surfaces may vary slightly based on the aircraft's configuration. The position of these control surfaces is presented in Figure 3.1 [50]. The fourth input, which is the throttle, is conveyed by the pilot directly to the engine, where it is used to generate thrust. An increase in throttle corresponds to a higher thrust output from the engine.

The system has six outputs with three corresponding to the attitudes of the aircraft (ϕ,θ,ψ), representing the roll, pitch, and yaw angles.The remaining three outputs describe the position of the aircraft with respect to the inertial frame (X,Y,Z).

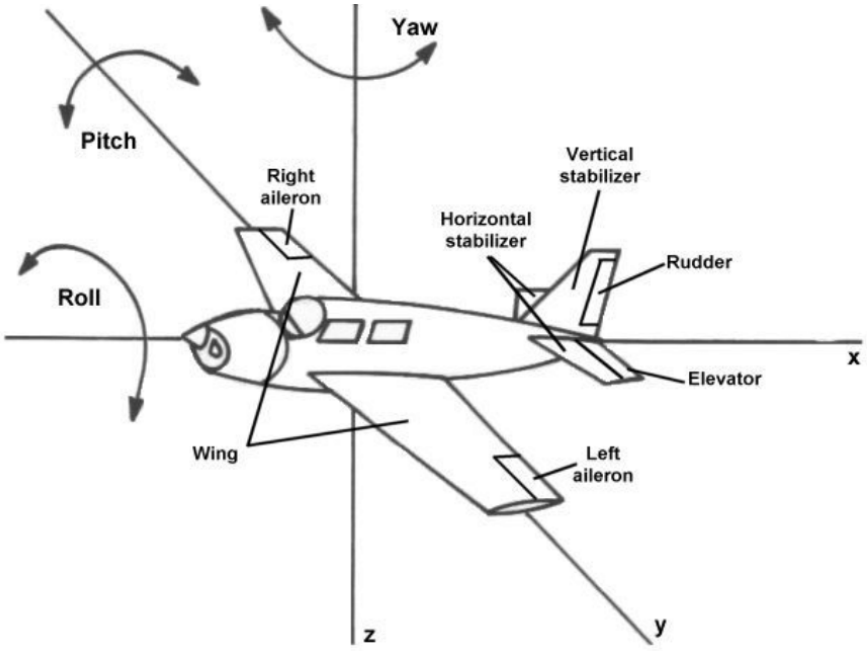

Figure 3.1: Aircraft's motion and control surfaces

3.2 Reference Frames and Coordinate systems

This section represents various reference frames and coordinate systems frequently employed for describing the motion of aircraft. The first one is the world reference frame, regarded as stationary relative to distant stars. It is utilized as a global reference for analyzing the motion of the vehicle, often denoted as the "inertial frame.". In the world frame, the z-axis is oriented

vertically downward, the x-axis points to the north, and the y-axis points eastward. The world frame is visualized in Figure 3.2 [51].

Next, there's the vehicle-carried frame, alternatively known as the North-East-Down (NED) frame, serving as a reference frame. The axes of the vehicle-carried frame align in the same directions as the inertial frame, the only distinction being that its origin is situated at the center of gravity of the aircraft.Consequently, it is utilized as a local reference for analyzing the motion of the vehicle. The transformation employed to transition forces or velocities from the vehicle-carried frame to the body frame is presented below:

$$R_{bv} = \begin{bmatrix} \cos\theta\cos\psi & \cos\theta\sin\psi & -\sin\theta \\ \sin\phi\sin\theta\cos\psi - \cos\phi\sin\psi & \sin\phi\sin\theta\sin\psi + \cos\phi\cos\psi & \sin\phi\cos\theta \\ \cos\phi\sin\theta\cos\psi + \sin\phi\sin\psi & \cos\phi\sin\theta\sin\psi - \sin\phi\cos\psi & \cos\phi\cos\theta \end{bmatrix}$$

After that, the body coordinate system, centered at the aircraft's center of gravity, is used to express the equations of motion. In this system, the x-axis aligns with the aircraft's nose, the y-axis aligns with the right wing, and the z-axis points downward along the plane of symmetry. The configuration of the body frame is illustrated in Figure 3.2. The following transformation is applied to transition from the inertial frame to body frame.

Finally, the wind coordinate system is used to present aerodynamic forces. This coordinate system is crucial since aerodynamic data, often obtained through wind tunnel testing, is typically presented in the wind coordinate system. Figure 3.3 [52] illustrates both the wind axis and the body axis coordinate systems. The subsequent transformation is applied to transition aerodynamic forces from the wind axis to the body axis.

$$R_{bw} = \begin{bmatrix} \cos\alpha\cos\beta & -\cos\alpha\sin\beta & -\sin\alpha \\ \sin\beta & \cos\beta & 0 \\ \sin\alpha\cos\beta & -\sin\alpha\sin\beta & \cos\alpha \end{bmatrix}$$

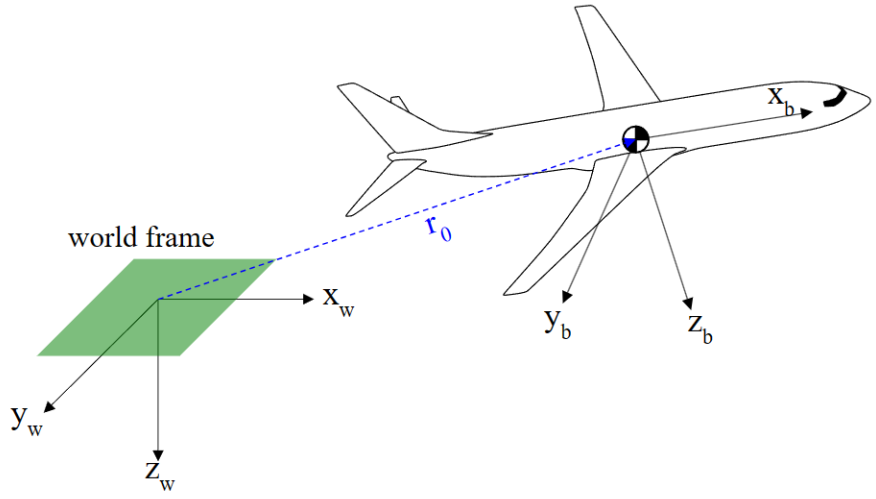

Figure 3.2: World frame and Body coordinate axis of a fixed-wing aircraft

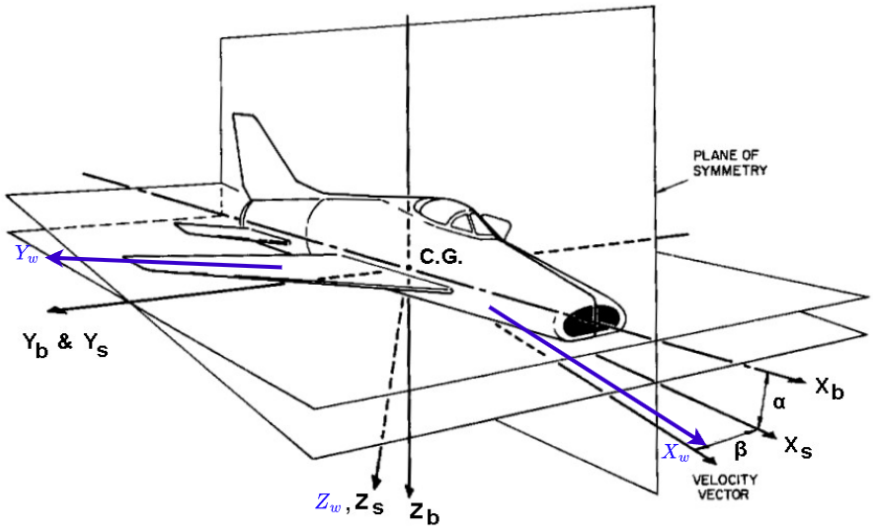

Figure 3.3: Wind axis and Body axis of fixed-wing aircraft

3.3 6-DOF Equations of Motion

The equations for modeling aircraft dynamics using 6DOF are established within the body-fixed coordinate system. The equations are obtained from [53] and [54]. The forces equations in the body-fixed coordinate system are defined as below:

$$\dot{u} = rv - qw - gsin\theta + \frac{X_A}{m} + \frac{T}{m} \tag{3.1}$$

$$\dot{v} = pw - ru + gcos\theta sin\phi + \frac{Y_A}{m} \tag{3.2}$$

$$\dot{w} = qu - pv + gcos\theta cos\phi + \frac{Z_A}{m} \tag{3.3}$$

The moment equations in the body-fixed coordinate system are defined as below:

$$\dot{p} = \frac{I_{zz}}{I_{eq}}(L + I_{xz}pq + (I_{yy} - I_{zz})qr) + \frac{I_{xz}}{I_{eq}}(N - (I_{yy} - I_{xx})pq - I_{xz}qr + H_e q) \tag{3.4}$$

$$\dot{q} = \frac{1}{I_{yy}}(M + I_{xz}(r^2 - p^2) + (I_{zz} - I_{xx})pr - H_e r) \tag{3.5}$$

$$\dot{r} = \frac{I_{xz}}{I_{eq}}(L + I_{xz}pq + (I_{yy} - I_{zz})qr) + \frac{I_{xx}}{I_{eq}}(N - (I_{yy} - I_{xx})pq - I_{xz}qr + H_e q) \tag{3.6}$$

where $I_{eq} = I_{zz}I_{xx} - I_{xz}^2$

To compute the roll, pitch, and yaw attitude angles of the aircraft based on its angular rates, a two-step transformation process is used. Initially, the angular rates are transformed into quaternions, and subsequently, the quaternions are transformed into Euler angles. Despite the availability of a direct transformation from angular rates to Euler angles, the preference is to use quaternions as they avoid the risk of gimbal lock. Gimbal lock represents the loss of one degree of freedom in specific Euler angle representations. This occurrence arises when two of the three rotational axes become aligned, leading to numerical instability and difficulty in representing certain orientations. In quaternions, this does not happen and that is why quaternions are used in this transformation. The kinematic equations for this transformation are shown below:

$$\dot{q} = \frac{1}{2}\begin{bmatrix} 0 & -p & -q & -r \\ p & 0 & r & -q \\ q & -r & 0 & p \\ r & q & -p & 0 \end{bmatrix}\begin{bmatrix} q_0 \\ q_1 \\ q_2 \\ q_3 \end{bmatrix}$$

$$\phi = \text{atan2}\left(2(q_0q_1 + q_2q_3), 1 - 2(q_1^2 + q_2^2)\right)$$
$$\theta = \sin^{-1}\left(2(q_0q_2 - q_3q_1)\right)$$
$$\psi = \text{atan2}\left(2(q_0q_3 + q_1q_2), 1 - 2(q_2^2 + q_3^2)\right)$$

3.4 Aerodynamic Model

Modeling the aerodynamics of an aircraft is crucial as it presents the forces and moments acting on the aircraft across its flight envelope. This knowledge serves as a guide to comprehend how the aircraft responds to varying angular rates, control surface deflections, angle of attack and sideslip angles.

The Computational Fluid Dynamics (CFD) values were acquired through conducting wind tunnel tests at low speeds, with the reference center of gravity positioned at $0.35\bar{c}$ [54]. The data from this study consists of 50 look-up tables and large intervals for angle of attack and sideslip angle, where ($-20^\circ \leq \alpha \leq 90^\circ$) and ($-30^\circ \leq \beta \leq 30^\circ$). Additionally, aerodynamic data are provided relative to additional control surfaces, specifically leading-edge flaps, and also relative to speed brakes. Due to the complexity of the given aerodynamic data, a simplified version is obtained from [55]. In this simplification, the leading-edge-flap and speed-brakes effects were excluded from the data. Additionally, the interval of alpha was updated to ($-20^\circ \leq \alpha \leq 45^\circ$). The simplified aerodynamic equations are presented below:

$$C_{X,t} = C_x(\alpha, \beta, \delta e) + \frac{\bar{c}q}{2V} C_{x_q}(\alpha) \tag{3.7}$$

$$\begin{aligned} C_{Y,t} = C_Y(\alpha, \beta) + \Delta C_{Y,\delta a=20} \frac{\delta a}{20} + \Delta C_{Y,\delta r=30} \frac{\delta r}{30} \\ + \frac{bp}{2V} C_{Y_p}(\alpha) + \frac{br}{2V} C_{Y_r}(\alpha) \end{aligned} \tag{3.8}$$

$$C_{Z,t} = C_z(\alpha, \beta, \delta e) + \frac{\bar{c}q}{2V} C_{z_q}(\alpha) \tag{3.9}$$

$$C_{l,t} = C_l(\alpha,\beta,\delta e) + \Delta C_{l,\delta a=20}(\frac{\delta a}{20}) + C_{l,\delta r=30}(\frac{\delta_r}{30}) + \frac{br}{2V}C_{l_r}(\alpha) + \frac{bp}{2V}C_{l_p}(\alpha) + \Delta C_{l_\beta}(\alpha)\beta \tag{3.10}$$

$$C_{m,t} = C_m(\alpha,\beta,\delta e) + C_{z,t}[x_{cg,ref} - x_{cg}] + \frac{\bar{c}q}{2V}C_{m_q}(\alpha) + \Delta C_m(\alpha) \tag{3.11}$$

$$C_{n,t} = C_n(\alpha,\beta,\delta e) - C_{Y,t}[x_{cg,ref} - x_{cg}]\frac{\bar{c}}{b} + \Delta C_{n,\delta a=20}(\frac{\delta a}{20}) + C_{n,\delta r=30}(\frac{\delta r}{30}) + \frac{br}{2V}C_{n_r}(\alpha) + \frac{bp}{2V}C_{n_p}(\alpha) + \Delta C_{n_\beta}(\alpha)\beta \tag{3.12}$$

As shown above, the aerodynamic data is initially obtained in non-dimensional form and is subsequently dimensionalized using specific equations. This process yields aerodynamic forces—namely lift, drag, and sideforce—as well as aerodynamic moments, which are roll, pitch, and yaw. The dimensionalizing equations are given as:

$$X_A = \frac{1}{2}\rho V^2 S C_{x,t} \tag{3.13}$$

$$Y_A = \frac{1}{2}\rho V^2 S C_{Y,t} \tag{3.14}$$

$$Z_A = \frac{1}{2}\rho V^2 S C_{Z,t} \tag{3.15}$$

$$L = \frac{1}{2}\rho V^2 S b C_{l,t} \tag{3.16}$$

$$M = \frac{1}{2}\rho V^2 S \bar{c} C_{m,t} \tag{3.17}$$

$$N = \frac{1}{2}\rho V^2 S b C_{n,t} \tag{3.18}$$

To be able to use the angle of attack, sideslip angle, and true airspeed in the calculation of aerodynamic coefficients, the following equations, expressed in terms of the aircraft's

velocity components, are used to determine each of these parameters.

$$V = \sqrt{u^2 + v^2 + w^2} \tag{3.19}$$

$$\alpha = tan^{-1}(\frac{w}{u}) \tag{3.20}$$

$$\beta = sin^{-1}(\frac{v}{V}) \tag{3.21}$$

3.5 Actuator Model

The servo motors are represented as first-order servos with a transfer function as follows:

$$\frac{1}{0.0495s + 1} \tag{3.22}$$

Following the servo motor model, a saturation component is introduced to represent the maximum surface deflection for each control surface. The deflection limits are as follows: 21.5° for the aileron, 25° for the elevator, and 30° for the rudder.

3.6 Propulsion Model

The propulsion system encompasses the engine responsible for generating the thrust essential to power the aircraft. The throttle, serving as the fourth input to the aircraft, is provided as an input to the engine. The amount of thrust generated by the engine is consequently influenced by the amount of the throttle given.

The engine being modeled is an afterburning turbofan jet engine, which is sourced from references [54] and [55]. To calculate the aircraft's thrust, three functions are employed: TGEAR, PDOT, and THRUST.

3.6.1 TGEAR Function

First, the throttle is given as input to the TGEAR function which makes use of the graph in [54] to convert the throttle command into a power command. This graph depicts a linear relationship between throttle and power until the military power level is reached, where the throttle value is 0.77. It is at this point that a change in the slope occurs, as illustrated in Figure 3.4 from [51].

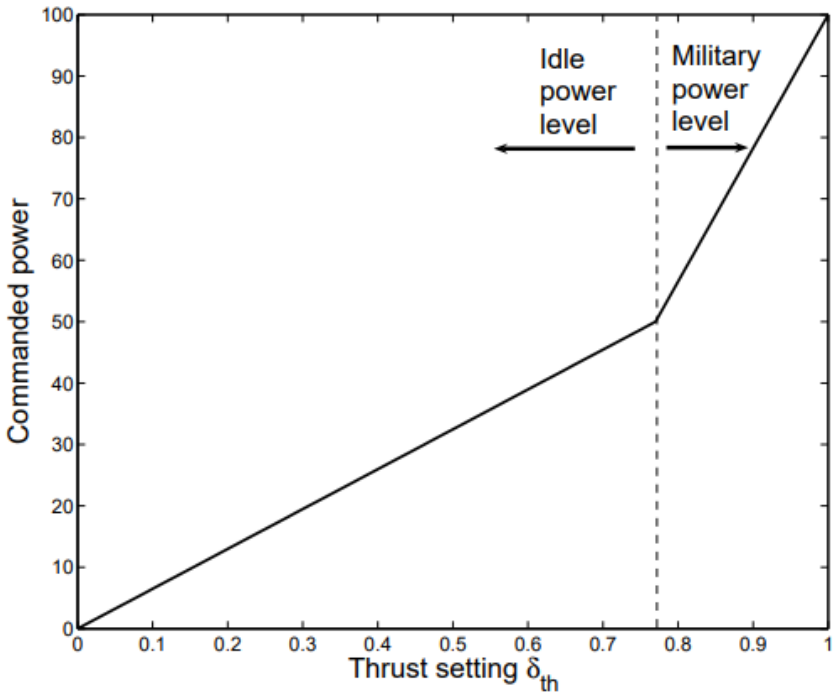

Figure 3.4: Relationship between the throttle input and the engine power level

3.6.2 PDOT Function

Subsequently, the PDOT function takes this calculated power command and the current actual power to determine the rate of power change within the engine. Figure 3.5 illustrates the sequential steps of the PDOT function. It can be seen in the flow chart that the PDOT function makes use of a rtau function, which is presented in Figure 3.6.

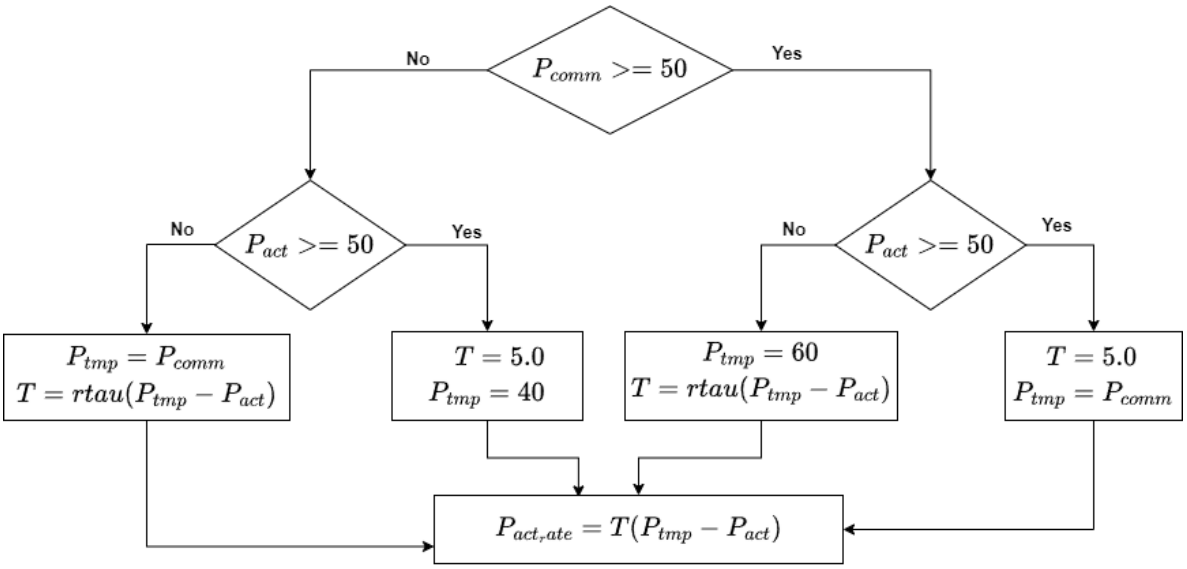

Figure 3.5: Flow chart of PDOT function

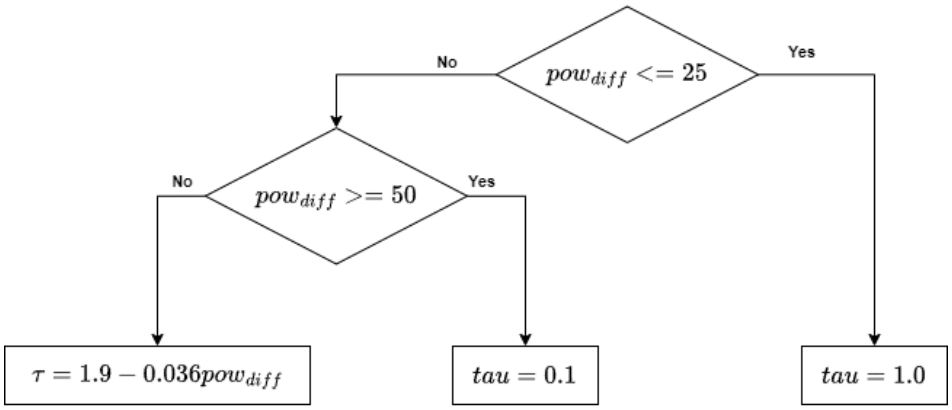

Figure 3.6: rtau function

3.6.3 THRUST Function

Finally, the rate of power change is integrated to yield the updated power value, which is then used as an input for determining the engine's thrust through the THRUST function. The steps of the THRUST function are outlined in the following pseudo code:

$$
\begin{aligned}
&\text{if } (P_{act} < 50) \\
&\quad \text{Thrust} = T_{\text{idle}} + (T_{\text{military}} - T_{\text{idle}}) \times P_{act} \times 0.02 \\
&\text{else} \\
&\quad \text{Thrust} = T_{\text{military}} + (T_{\text{max}} - T_{\text{military}}) \times (P_{act} - 50) \times 0.02
\end{aligned}
$$

In this function, T_{idle}, $T_{military}$, and T_{max} are the outputs of Lookup tables in [54] which take as input the altitude and Mach of the aircraft and yields the corresponding Thrust values as outputs.

3.7 Atmospheric Model

The atmospheric model is a crucial element for achieving a realistic simulation since it provides key variables essential for the model. The following subsections show the components of the atmospheric model.

3.7.1 ISA Atmosphere Model

The Simulink ISA Atmosphere Model block is used to derive air density. Given the varying altitude of the fixed-wing UAV across the flight envelope, maintaining accurate density calculations throughout the simulation is crucial. This is necessary because air density decreases with increasing altitude. The model takes altitude as input and yields the corresponding air density.

3.7.2 WGS84 Gravity Model

The Simulink WGS84 Gravity Model block provides the gravity term 'g'. Similar to air density, g value decreases as altitude increases. However,the rate of change of the gravity term

with respect to altitude is considerably lower when compared to that of the air density. Although there is a minimal change of the gravity term throughout the simulation, the inclusion of WGS84 is added to maintain realistic atmospheric conditions. The model takes as input the aircraft's latitude, longitude, and altitude as input, producing the gravity term, 'g'.

3.7.3 Dryden Wind Turbulence Model

To assess the robustness of the proposed controllers by incorporating wind disturbance, the Dryden Wind Turbulence Model is employed. The model obtains wind disturbance through passing band-limited white noise through suitable shaping filters. This block follows the mathematical representation outlined in the Military Specification MIL-F-8785C [56]. The model takes the aircraft's altitude, airspeed, and DCM matrix as input, yielding wind velocities and angular rates.

The fixed-wing nonlinear dynamic model constructed in Simulink/MATLAB environment is illustrated in Figure 3.7.

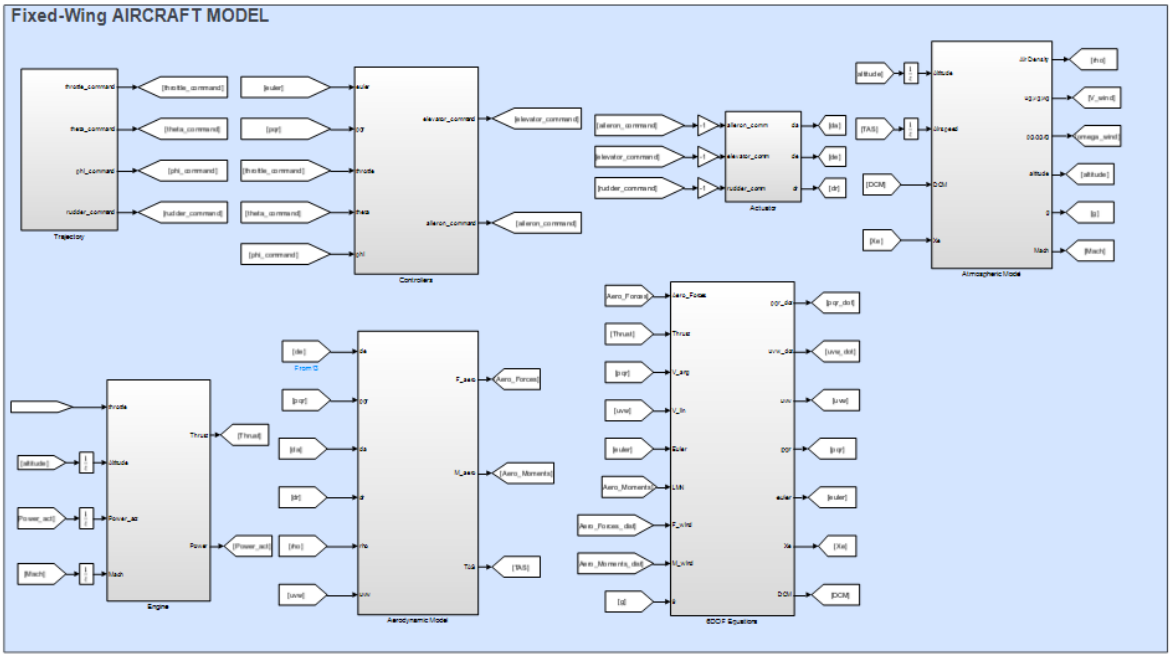

Figure 3.7: Simulink Model of fixed wing UAV

CHAPTER 4

ROBUST CONTROLLERS DESIGN USING ACTIVE DISTURBANCE CANCELLATION

In this chapter, different approaches to designing controllers for the fixed-wing UAV are examined. More precisely, this section offers detailed insights into a gain-scheduled controller, a disturbance observer-based controller using a gain-scheduled controller as baseline controller, an integral sliding mode controller, and a disturbance observer-based controller using the integral sliding mode controller as a baseline controller.

4.1 Gain Scheduling

Gain scheduling is a control strategy that involves adjusting the parameters or gains of a controller based on changes in the operating conditions or the characteristics of the system being controlled. This approach is often employed when the dynamics of the system vary significantly under different operating conditions, and a fixed controller may not perform

optimally across the entire operating range. Gain scheduling offers a compromise between fixed and adaptive control. Instead of continuously adapting the controller gains, it uses a set of pre-defined gain schedules that are selected based on specific operating conditions or system states.

When the system operates in a region between predefined operating conditions, gain scheduling often involves interpolating between the nearest pre-defined gain sets. In summary, gain scheduling is a practical approach to address the challenges posed by systems with varying dynamics. It allows for improved control performance across different operating conditions without the computational complexity of real-time adaptive control.

In the control architectures of Fixed-Wing UAVs, gain scheduling assumes a significant role. This is attributed to the diverse operating points inherent in Fixed-Wing UAVs, characterized by varying airspeeds and altitudes. Consequently, employing a fixed set of controller gains is impractical across the entirety of the flight envelope. A prominent example illustrating this is the PixHawk autopilot, one of the most renowned Fixed-Wing UAV autopilots. The PixHawk system employs a cascaded gain-scheduled controller based on PID for attitude control. The cascaded control system comprises an outer loop for attitude and an inner loop for angular rates. The resulting output from this controller design is the command given to the control surfaces. For pitch attitude control, it is the elevator command, and for roll attitude control, it is the aileron command. The approach to gain scheduling in this autopilot relies on airspeed scaling. Essentially, a gain value is multiplied by the PID controller gains, with this gain value adjusting according to the true airspeed. This adaptive mechanism ensures the proportional scaling of the PID gain controllers based on the current airspeed conditions [57].

The gain scheduling methodology for Fixed-Wing UAVs is not confined solely to airspeed values. Furthermore, it is not limited to a singular gain value multiplied by all controller parameters. The approach to gain scheduling proposed in this study depends on throttle input given by the pilot rather than airspeed. Additionally, instead of relying on a single gain value to be multiplied by all controller gains, a lookup table is implemented. This lookup table yields the controller gain values corresponding to the specific throttle input value.

The values used in the lookup tables, depending on the throttle input, are designed accord-

ing to three distinct operating points of the aircraft. Each operating point signifies a unique trim point, encompassing steady-level flight at sea level, pull-up flight, and steady-level flight at an altitude of 600 m. The controller parameters are individually tuned for each flight stage, and subsequently, the lookup tables are constructed based on the tuned parameter values.

The gain-scheduled casacded controller architecture implemented for this study is for pitch and roll attitudes. Figures 4.1 and 4.2 depict the implementation of the cascaded controllers for pitch and roll attitudes, respectively.

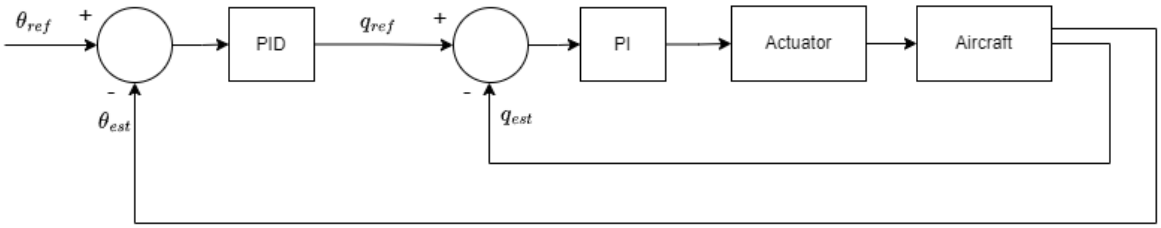

Figure 4.1: Pitch attitude cascaded control system

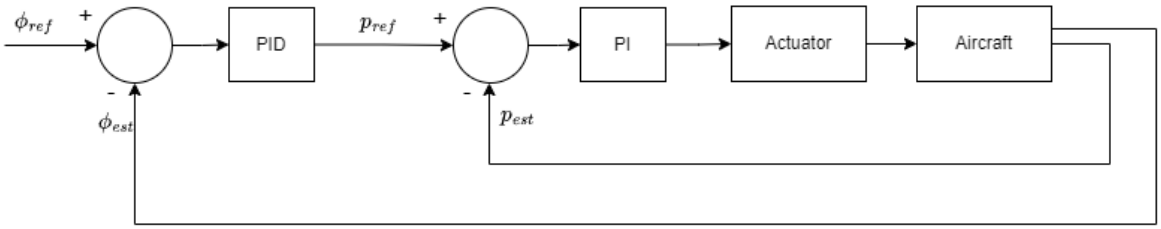

Figure 4.2: Roll attitude cascaded control system

4.2 Conditional Integral Sliding Mode Controller

Sliding mode controller is a nonlinear control system that involves designing a function, known as the sliding variable, based on the system's error. The primary objective is to drive this sliding variable to zero. Once the sliding variable reaches zero, a specifically designed sliding surface is introduced. The system's trajectory is then constrained to follow this sliding

surface. The sliding variable equation in terms of the system's error is given as

$$\sigma = \dot{e} + ce \ , \quad c > 0 \tag{4.1}$$

Meanwhile, the controller input is given as

$$u = \rho sgn(\sigma) \tag{4.2}$$

where ρ is the controller gain.

The signum function is defined by,

$$\text{sgn}(u) = \begin{cases} 1, & \text{if } u > 0, \\ -1, & \text{if } u < 0. \end{cases} \tag{4.3}$$

The continuous fluctuation between 1 and -1 of the signum function is the reason for the chattering problem observed in the conventional sliding mode controller. A common approach to solve this problem is to replace the discontinuous signum function with its continuous approximation, the saturation function $sat(\frac{s}{\mu})$, which is defined by,

$$\text{sat}(u) = \begin{cases} u, & \text{if } |u| \leq 1, \\ \text{sgn}(u), & \text{if } |u| > 1. \end{cases} \tag{4.4}$$

This method however causes non-zero steady-state error, which is proportional to μ. μ value should be reduced to obtain smaller steady-state error, however that comes at the cost of causing chattering again.

With the aim of enhancing the sliding mode controller performance, various modified versions of the sliding mode controller were proposed by researchers. For instance, there is the conventional first-order sliding mode controller, characterized by a single sliding surface. Another type is the second-order sliding mode controller, consisting of a second-order sliding surface. Higher-order sliding mode controllers, featuring higher orders of sliding surfaces, are also present. Additionally, there is the super-twisting sliding controller, specifically de-

signed to manage disturbances and uncertainties more efficiently when contrasted with the conventional sliding mode controller. Also, there is integral sliding mode controllers which incorporate integral action to the controller in order to eliminate steady state errors. [32].

Among the above mentioned sliding mode controller types, the integral sliding mode controller offers a solution to the steady-state error problem faced by the continuous sliding mode controller. It provides asymptotic stability to the system, which implies that the system's states converge to the desired values as time approaches infinity, ensuring long-term stability and performance. The integrator augmented to the system is based on the system's tracking error, which is given by

$$\dot{\sigma} = e \tag{4.5}$$

Unfortunately, this asymptotic stability realized by the integral action comes at the expense of degrading the transient performance. Addressing this challenge, Seshagiri and Khalil [58] introduce a novel form of integral sliding mode controller. Their approach involves an integral sliding mode controller derived from the continuous sliding mode controller. Unlike the traditional integral sliding mode controller, their proposal incorporates a "conditional integrator." This distinctive feature ensures that the integrator operates only after the system reaches steady-state, meanwhile it does not operate during transient response. Consequently, this design preserves the transient response characteristics of the ideal sliding mode controller without integral control. For this approach, the sliding surface equation is given as

$$s = k_0\sigma + e \tag{4.6}$$

where $k_0 > 0$ is arbitrary, and σ is the output of

$$\dot{\sigma} = -k_0\sigma + \mu sat(\frac{s}{\mu}) \,, \quad \sigma(0) = 0 \tag{4.7}$$

The implementation of the conditional integral sliding mode controller in this study is based on [59], where the controller is applied to the longitudinal dynamics of F-16 aircraft. Specifically, the control input, representing the elevator in this context, is derived by utilizing the pitch angular velocity as the system's tracking error for the sliding variable. The control

input is given by the following equation:

$$\delta e = -ksat(\frac{s}{\mu}) = -ksat(\frac{k_0\sigma + e}{\mu}) \tag{4.8}$$

In this study, the sliding mode controller is only applied to the longitudinal dynamics. Meanwhile, the lateral dynamics, particularly the roll attitude, are controlled through the gain-scheduled controller presented in the preceding section.

4.3 Disturbance Observer

Conventional feedback-control systems, like PID controllers, regulate disturbances at a comparatively slow pace through feedback regulation. On the other hand, feedforward control offers an efficient method for prompt disturbance compensation. However, implementing traditional feedforward control necessitates the measurement of disturbances using sensors. In many cases, it is challenging or even impossible to measure disturbances through sensors, limiting the development of traditional feedforward control in control engineering [41].

Disturbance observers offer an effective technique for estimating disturbances across various systems. Disturbance Observer-Based Control (DOBC) stands out as a promising approach for disturbance attenuation. DOBC integrates a baseline feedback controller, such as gain-scheduled controllers, with a disturbance observer-based compensation to enhance the robustness and disturbance attenuation of the baseline controller. The block diagram of DOBC is depicted in Figure 4.3 where u represents the input from the feedback controller, y is the output of the system, d stands for the external disturbance, and ζ denotes the sensor noise. $C(s)$ is the feedback controller, $G(s)$ is the plant, $G_n(s)$ is the nominal plant, and $Q(s)$ is the filter of the disturbance observer.

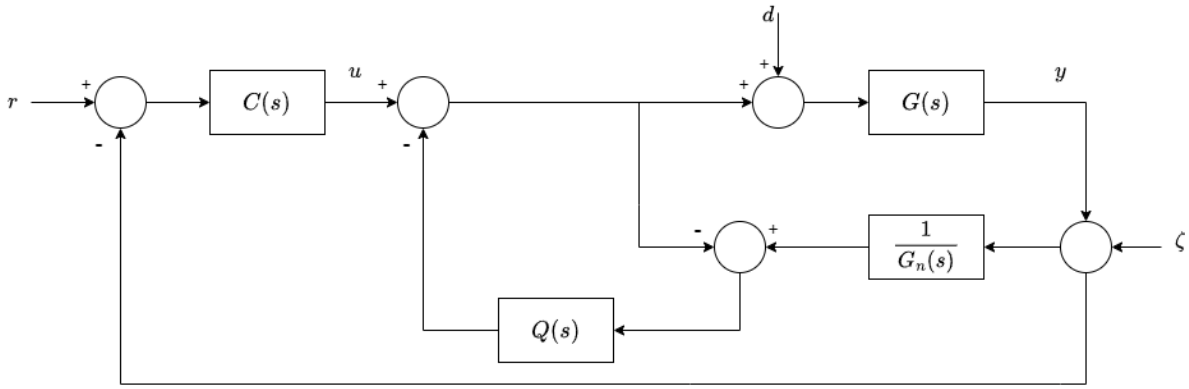

Figure 4.3: Block diagram of DOBC

However, the DOBC depicted in Figure 4.3 represents a non-realizable system due to the term $\frac{1}{G_n(s)}$. Consequently, the system is revised to a realizable form, as illustrated in Figure 4.4 .

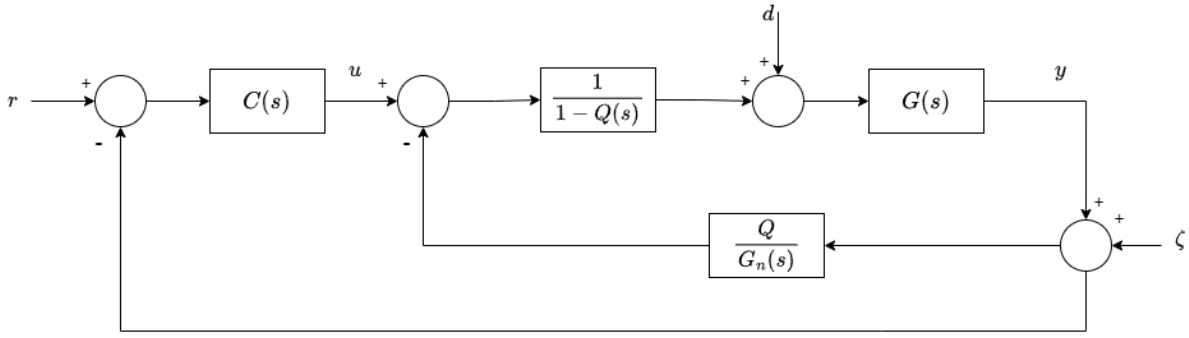

Figure 4.4: Block diagram of realizable DOBC

The DOBC can be expressed using the following equations

$$Y(s) = T_{dy}(s)D(s) + T_{uy}(s)U(s) + T_{\zeta y}(s)\zeta(s) \tag{4.9}$$

where,

$$T_{dy}(s) = \frac{(1-Q(s))G(s)G_n(s)}{Q(s)(G(s)-G_n(s))+G_n(s)} \tag{4.10}$$

$$T_{uy}(s) = \frac{G(s)G_n(s)}{Q(s)(G(s)-G_n(s))+G_n(s)} \tag{4.11}$$

$$T_{\zeta_y}(s) = \frac{G(s)Q(s)}{Q(s)(G(s) - G_n(s)) + G_n(s)} \tag{4.12}$$

The filter transfer function $Q(s)$ plays a crucial role in the function of the disturbance observer. In the scenario where $Q(s) = 1$ the numerator of function (4.10) becomes zero, resulting in the cancellation of disturbances. Simultaneously, function (4.11) equates to the nominal plant $G_n(s)$, signifying that the nominal plant matches with the actual plant. Additionally, in equation (4.12), the transfer function becomes one, indicating that sensor noise remains unaffected by the disturbance observer; thus, the observer cannot nullify the impact of sensor noise ζ.

The filter used in the implemented disturbance observer is a first-order low-pass filter with a cutoff frequency of 10 rad/s. The transfer function of the low-pass filter is given as

$$G(s) = \frac{\omega_c}{s + \omega_c} = \frac{10}{s + 10} \tag{4.13}$$

The block diagram of the disturbance observer implemented in the thesis is illustrated in Figure 4.5 [60], where $i = 1, 2, ..6$ and the symbols depicted in the figure are represented by the following equations.

$$M_{nom} = \begin{bmatrix} m & 0 & 0 & 0 & 0 & 0 \\ 0 & m & 0 & 0 & 0 & 0 \\ 0 & 0 & m & 0 & 0 & 0 \\ 0 & 0 & 0 & Ixx & 0 & -Ixz \\ 0 & 0 & 0 & 0 & Iyy & 0 \\ 0 & 0 & 0 & -Izx & 0 & Izz \end{bmatrix}$$

$$f = \begin{bmatrix} X_A + T - mg\sin\theta \\ Y_A + mg\sin\phi\cos\theta \\ Z_A + mg\cos\phi\cos\theta \\ L \\ M \\ N \end{bmatrix}$$

$$\tau_{dist} = \begin{bmatrix} 0 \\ 0 \\ 0 \\ 0 \\ -H_e r \\ H_e q \end{bmatrix} + \begin{bmatrix} F_{w_x} \\ F_{w_y} \\ F_{w_z} \\ M_{w_x} \\ M_{w_y} \\ M_{w_w} \end{bmatrix} + \begin{bmatrix} C_1 \\ C_2 \end{bmatrix}$$

where,

$$C_1 = \begin{bmatrix} p \\ q \\ r \end{bmatrix} \times \begin{bmatrix} u \\ v \\ w \end{bmatrix} \qquad C_2 = \begin{bmatrix} p \\ q \\ r \end{bmatrix} \times \begin{bmatrix} Ixx & 0 & -Ixz \\ 0 & Iyy & 0 \\ -Izx & 0 & Izz \end{bmatrix} \begin{bmatrix} p \\ q \\ r \end{bmatrix}$$

In the provided equations, M_{nom} presents the mass-inertia matrix, while f represents the inputs of the disturbance observer, encompassing aerodynamic forces and moments derived from the aerodynamic model, along with thrust from the propulsion model. τ_{dist} accounts for wind disturbances and nonlinearities within the system. The first vector illustrates the gyroscopic effect, the second vector characterizes the wind-induced forces and moments, and the third vector presents the Coriolis effect.

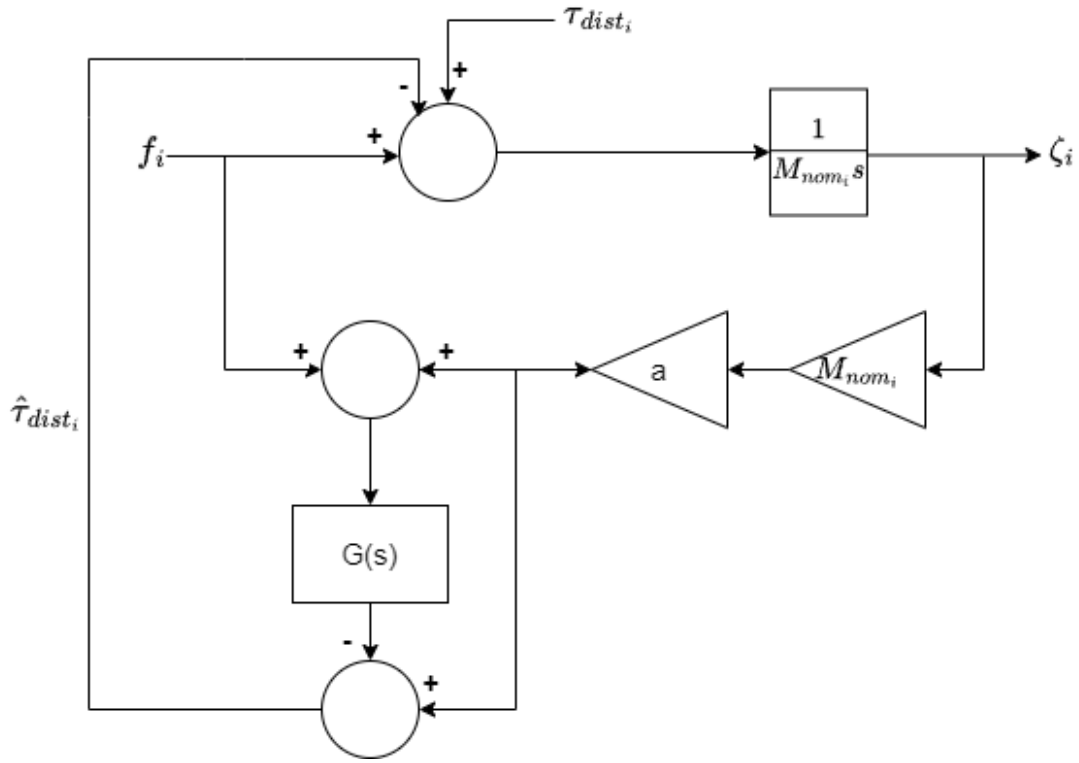

Figure 4.5: Disturbance observer implementation

CHAPTER 5

SIMULATION RESULTS

This chapter provides simulation results and discussion of the flight envelope covered by the UAV using gain-scheduled controller, conditionally integral sliding mode controller, and disturbance observer-based controllers. The flight envelope encompasses three stages: firstly, a steady-level wing flight at sea level; secondly, a pull-up flight, and finally, a steady-level wing flight at an altitude of 600 meters.

Following the assessment of each controller's performance, a comprehensive comparison is undertaken among the proposed controller architectures. This comparative analysis ultimately leads to a determination of which controller is most suitable for implementation in Fixed-wing UAV autopilots.

5.1 Model Parameters

The simulation parameters, such as mass, moment of inertia, and wing dimensions are shown in Table 5.1 [54]. The aerodynamic and engine data utilized in the model are obtained from [55].

Symbol	Magnitude
$\bar{c}$	$3.45\,m$
b	$9.144\,m$
S	$27.87\,m^2$
m	$9298\,kg$
I_{xx}	$12875\,kg \cdot m^{-2}$
I_{yy}	$75674\,kg \cdot m^{-2}$
I_{zz}	$85552\,kg \cdot m^{-2}$
I_{xz}	$1331\,kg \cdot m^{-2}$
H_e	$1331\,kg \cdot m^2/s$

Table 5.1: Simulation parameters

5.2 Gain-Scheduled Controller

In the first simulation, the gain-scheduled controller, based on the tuned PID controller, is used to control the Fixed-wing UAV. As demonstrated in the preceding section, a cascaded controller structure was used to control both the longitudinal dynamics, based on the pitch attitude, and the lateral dynamics, based on the roll attitude. It should be noted that no external disturbances were introduced during this simulation. The reason for this is to evaluate the baseline performance, which means that the performance of the control system should be examined under nominal conditions.

Tables 5.2,5.3 present the tuned set of gains for the pitch controller for each flight stage, while Tables 5.4,5.5 present the tuned set of gains used in the roll controller for each flight stage. These gain values constitute the entries used in the look-up tables for gain-scheduling. Figures 5.1-5.7 show the results of the first simulation.

flight stage	K_P	K_I	K_D
wing-level flight at sea level	6	0.1	0
pull-up flight	10	0.3	0.2
wing-level flight at 600 m	9	0.2	0

Table 5.2: Pitch angle controller gains

flight stage	K_P	K_I
wing-level flight at sea level	1	0.05
pull-up flight	2	0.25
wing-level flight at 600 m	0.3	0.2

Table 5.3: Pitch rate controller gains

flight stage	K_P	K_I	K_D
wing-level flight at sea level	1	0	0.7
pull-up flight	0.5	0	0
wing-level flight at 600 m	1	0	0.1

Table 5.4: Roll angle controller gains

flight stage	K_P	K_I
wing-level flight at sea level	1	0
pull-up flight	1	0
wing-level flight at 600 m	0.5	0

Table 5.5: Roll rate controller gains

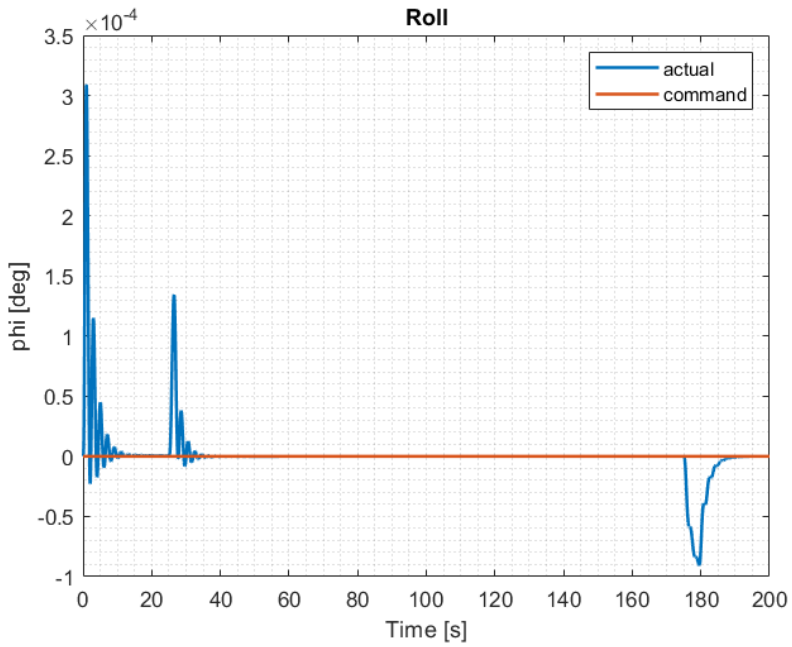

Figure 5.1: Roll attitude using gain-scheduled controller

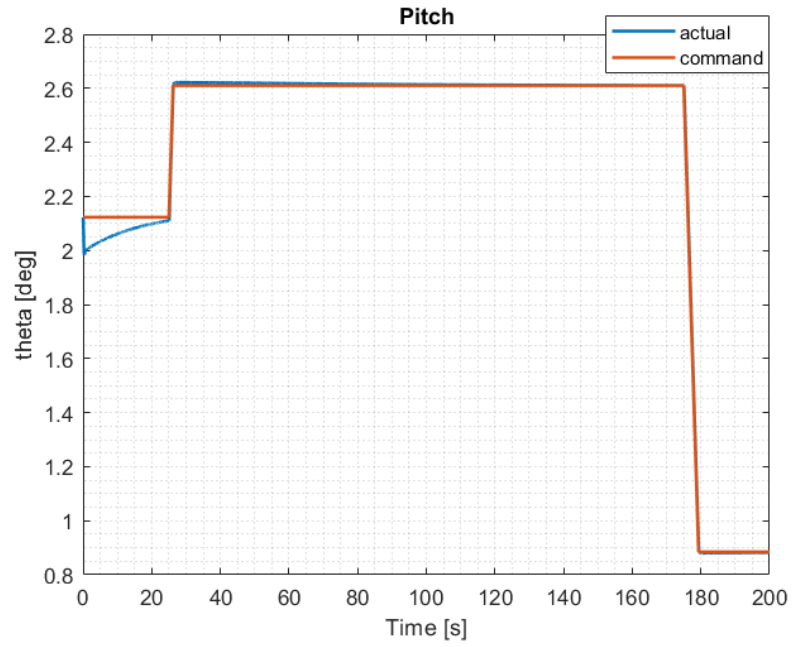

Figure 5.2: Pitch attitude using gain-scheduled controller

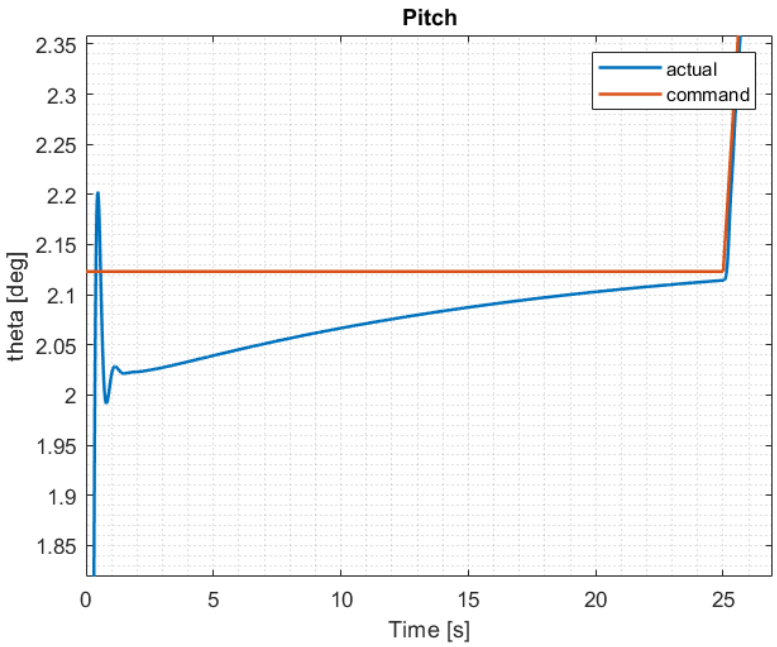

Figure 5.3: Pitch attitude of the first flight stage using gain-scheduled controller

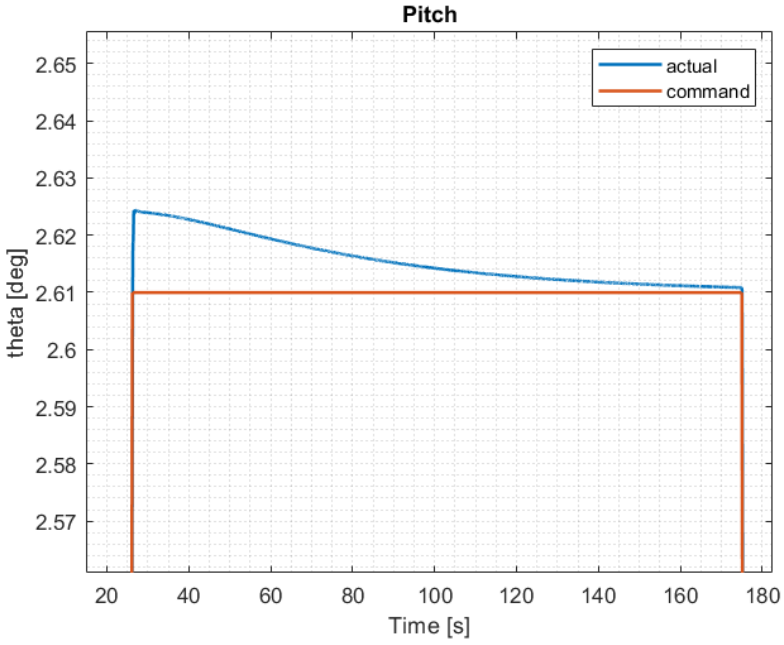

Figure 5.4: Pitch attitude of the second flight stage using gain-scheduled controller

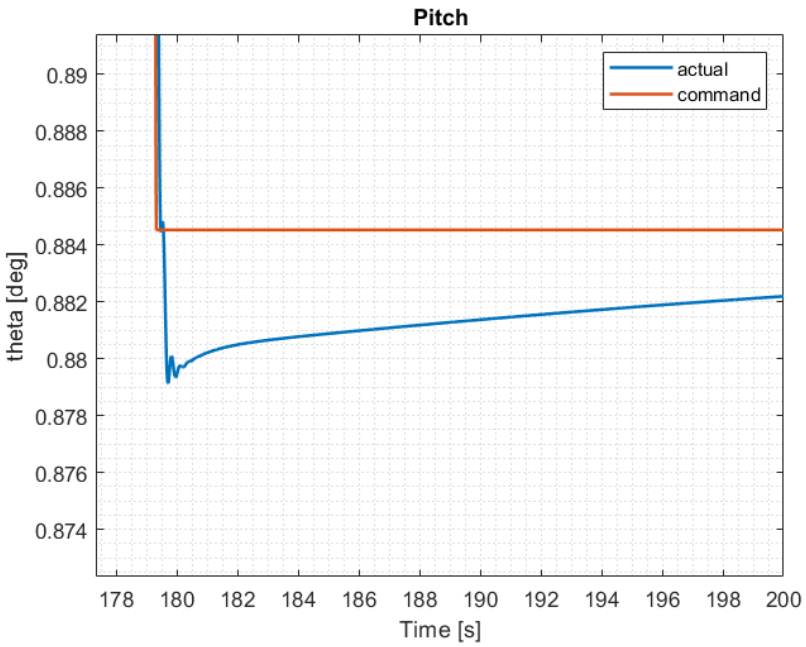

Figure 5.5: Pitch attitude of the third flight stage using gain-scheduled controller

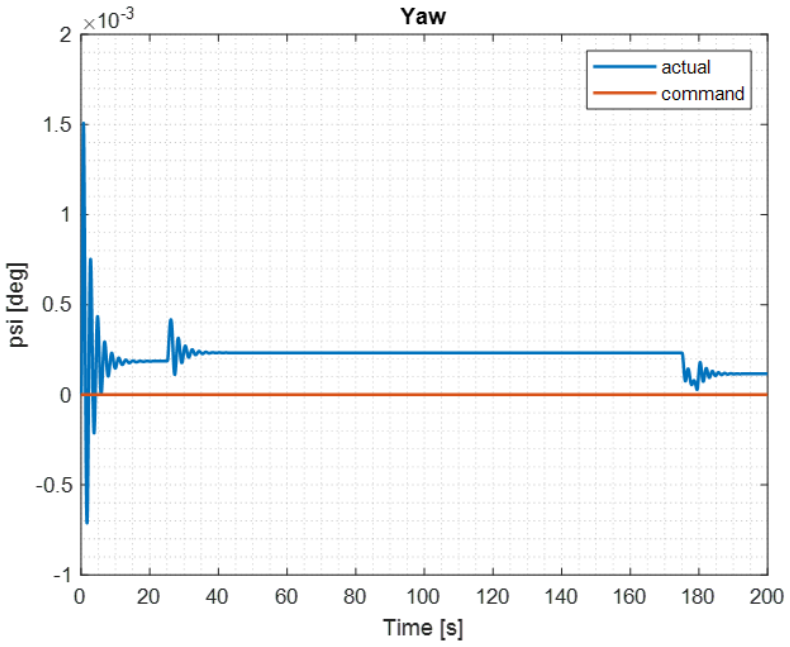

Figure 5.6: Yaw attitude using gain-scheduled controller

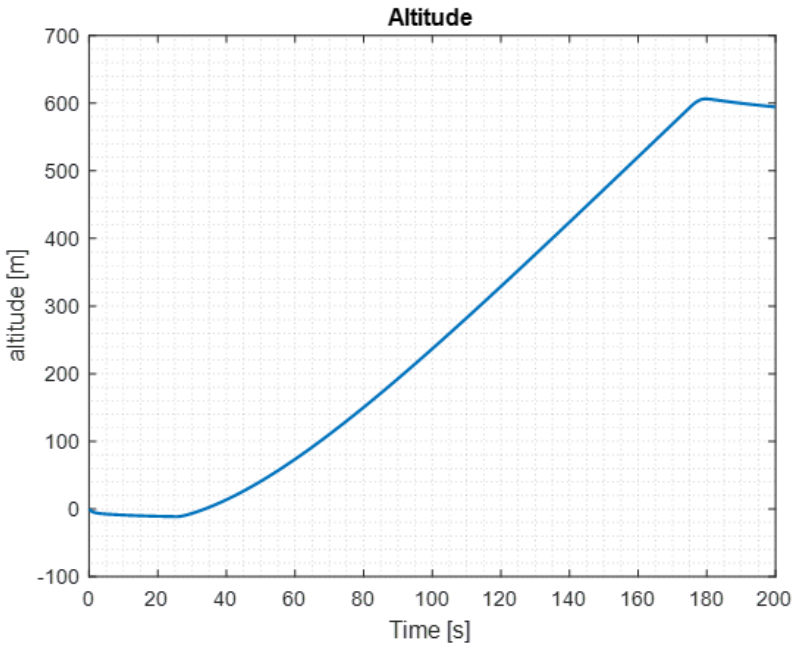

Figure 5.7: Altitude using gain-scheduled controller

In Figures 5.1 and 5.6, noticeable oscillations occur at specific time points, namely 25 seconds and 175 seconds. These oscillations coincide with transitions in the flight stages of the UAV. At 25 seconds, the UAV shifts from steady-level flight to a pull-up flight, and at 175 seconds, it undergoes a second stage change, transitioning from pull-up flight to steady-level flight at an altitude of 600 meters.

During these stage changes, there is an inherent alteration in the pitch angle, consequently leading to a change in the pitch angular velocity. This variation is evident in Figure 5.2.

Through examining the 6 DOF equations of motion, it becomes apparent that the pitch angular velocity is a key factor in computing states related to lateral motion. These states, in turn, contribute to the determination of roll and yaw angles as depicted in Figures 5.1 and 5.6. Thus, the change in pitch angular velocity during the specified time instances induce the observed oscillatory patterns in both roll and yaw attitudes.

Analyzing the close-up graphs provided in Figures 5.3-5.5, derived from Figure 5.2, it becomes evident that the gain-scheduled controller effectively tracks the pitch reference, resulting in the desired performance. This observation is further supported by Figure 5.7, which illustrates steady-level flight for the initial 25 seconds, followed by an increase in altitude

during the pull-up stage. Also, the UAV successfully maintains steady-level flight during the final stage, which takes place from 175 seconds to 200 seconds.

5.3 Gain-Scheduled Controller Under Fixed Disturbance

In this simulation, a constant disturbance is introduced to the system to assess the performance of the gain-scheduled controller under a fixed disturbance scenario. Specifically, the fixed disturbance is applied solely to the longitudinal motion, with no impact on the lateral motion.

The fixed disturbance is deliberately incorporated into the elevator control output, through the addition of 3 degrees to the elevator command from the controller. This modified command is then fed into the actuator and subsequently to the UAV's aerodynamic model, contributing to the computation of aerodynamic forces and moments.

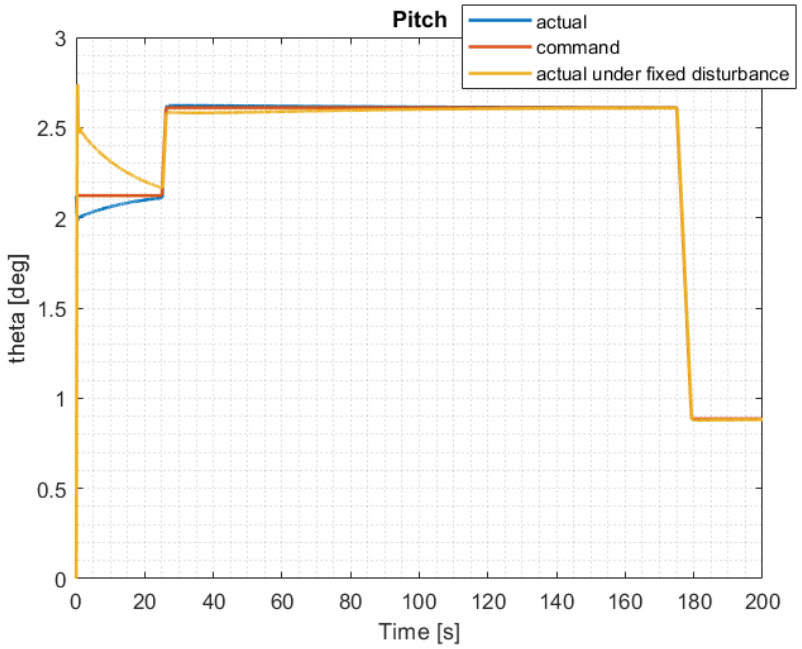

Figure 5.8: Pitch attitude using gain-scheduled controller under fixed disturbance

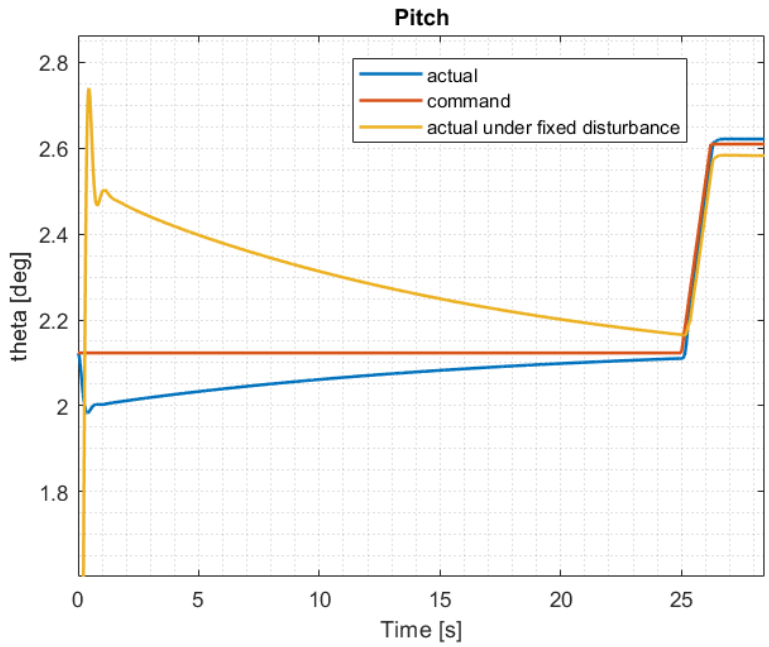

Figure 5.9: Pitch attitude of the first flight stage using gain-scheduled controller under fixed disturbance

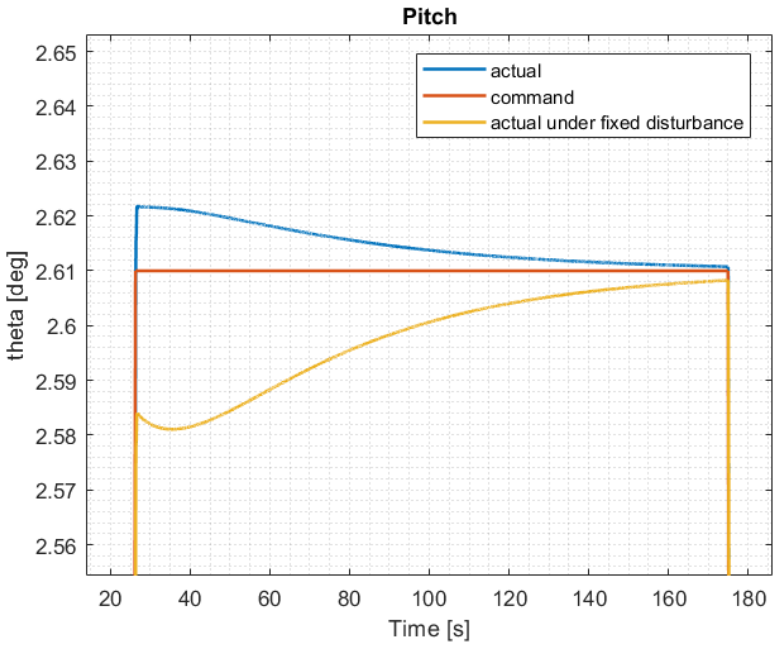

Figure 5.10: Pitch attitude of the second flight stage using gain-scheduled controller under fixed disturbance

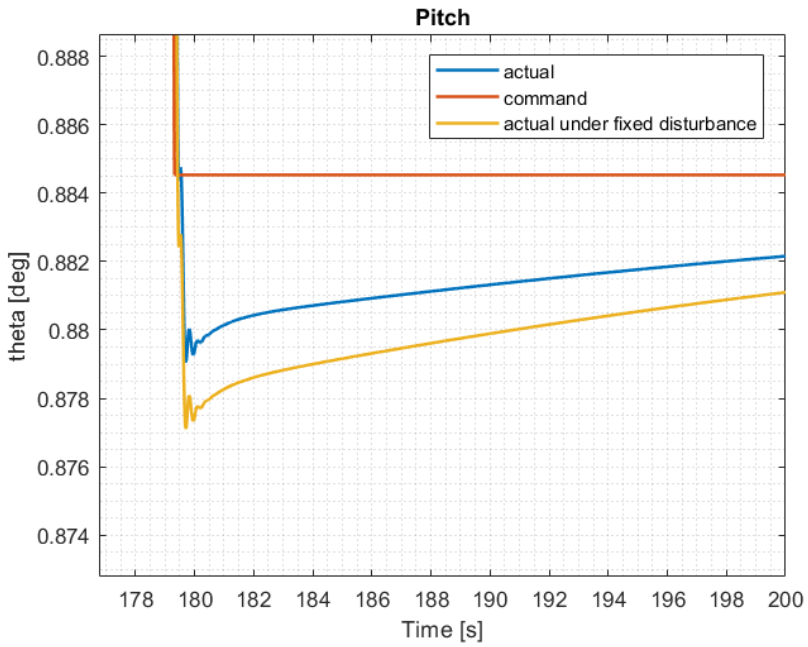

Figure 5.11: Pitch attitude of the third flight stage using gain-scheduled controller under fixed disturbance

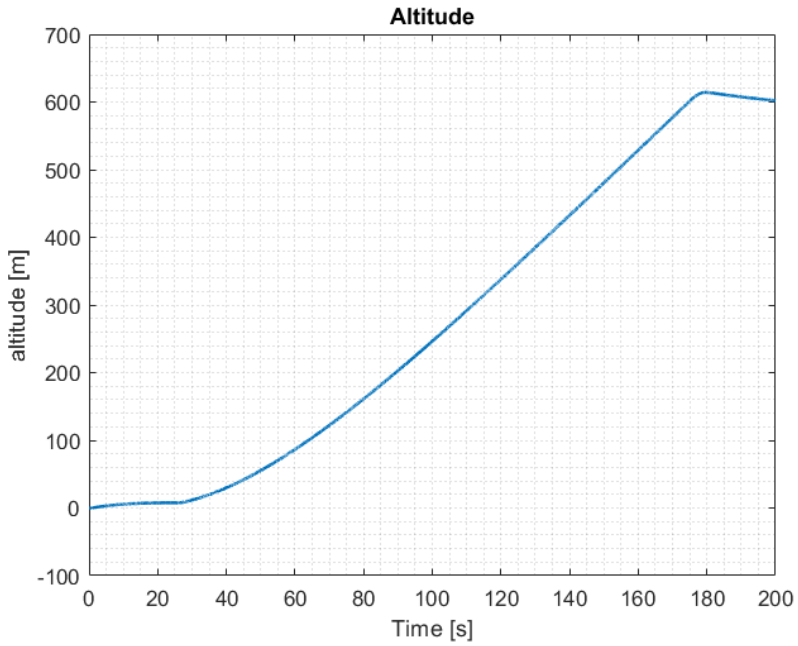

Figure 5.12: Altitude using gain-scheduled controller under fixed disturbance

Since the fixed disturbance exclusively influences the longitudinal dynamics of the aircraft, the graphs in this section present only the pitch and altitude graphs. Notably, the roll

and yaw attitudes remain unaffected, and therefore, are not shown in this analysis.

Upon examining the pitch attitude and altitude graphs and comparing them with the gain-scheduled controller's performance under nominal conditions, an obvious deterioration in the controller's performance becomes evident following the introduction of a fixed disturbance to the elevator command. Notably, there is no recognizable alteration in the altitude graph after the introduction of the fixed disturbance.

Furthermore, it can be seen that the performance in the second and third flight stages improves in comparison to the first stage. This improvement is attributed to the presence of the integrator, which gradually compensates for the impact of the fixed disturbance introduced to the model.

The subsequent tables provide a detailed comparison of RMSE, maximum, and minimum errors between the UAV in nominal conditions and when subjected to the fixed disturbance, with each table corresponding to a specific flight stage.

Disturbance	RMSE	$\lvert E_{min} \rvert$	$\lvert E_{max} \rvert$
No disturbance	0.0581	0.0129	0.1099
Fixed disturbance	0.1780	0.0423	0.3371

Table 5.6: First flight stage pitch attitude errors under fixed disturbance

Disturbance Case	RMSE	$\lvert E_{min} \rvert$	$\lvert E_{max} \rvert$
No disturbance	0.0060	7.8734e-04	0.0120
Fixed disturbance	0.0154	0.0017	0.0354

Table 5.7: Second flight stage pitch attitude errors under fixed disturbance

Disturbance Case	RMSE	$\lvert E_{min} \rvert$	$\lvert E_{max} \rvert$
No disturbance	0.0033	0.0024	0.0049
Fixed disturbance	0.0048	0.0034	0.0068

Table 5.8: Third flight stage pitch attitude errors under fixed disturbance

Examining Tables 5.6-5.8 reveals a consistent trend across all flight stages: the error

notably increases when the UAV operates under the influence of a fixed disturbance. The most substantial difference from the nominal case is predominantly evident in the first flight stage. Subsequently, while the error difference between the two cases diminishes, the fixed disturbance scenario consistently exhibits higher root mean square error (rmse), minimum, and maximum errors throughout the flight stages.

5.4 Gain-Scheduled Controller Under Wind Disturbance

Rather than incorporating a fixed disturbance in this simulation, a more realistic type of disturbance is employed. Utilizing the Dryden model available in Simulink, wind disturbance is introduced into both longitudinal and lateral motions of the model. The Dryden model generates linear and angular wind velocities in the aircraft's body axis, and these are subsequently added to the linear and angular velocities of the aircraft, which serve as inputs for the aerodynamic model. Figure 5.13 illustrates the procedure for introducing wind, where (omega wind) represents the angular velocities of the wind, and (V wind) represents the linear velocities of the wind. The outputs from the aerodynamic model encompass aerodynamic forces and moments, incorporating the wind disturbance, and are subsequently fed as inputs into the equations of motion block. Figures 5.14-5.15 present the wind velocities added to the model.

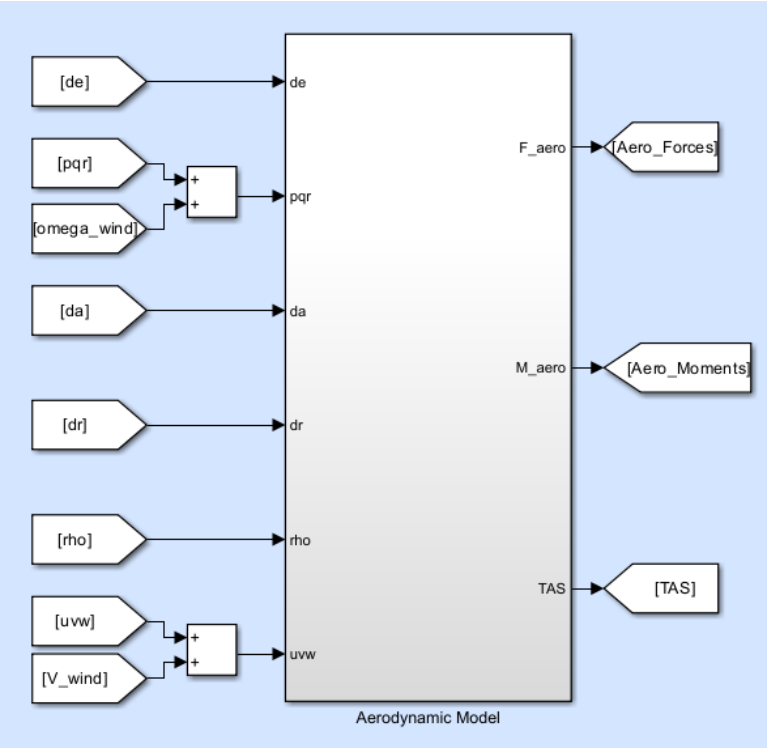

Figure 5.13: Incorporation of wind into the model

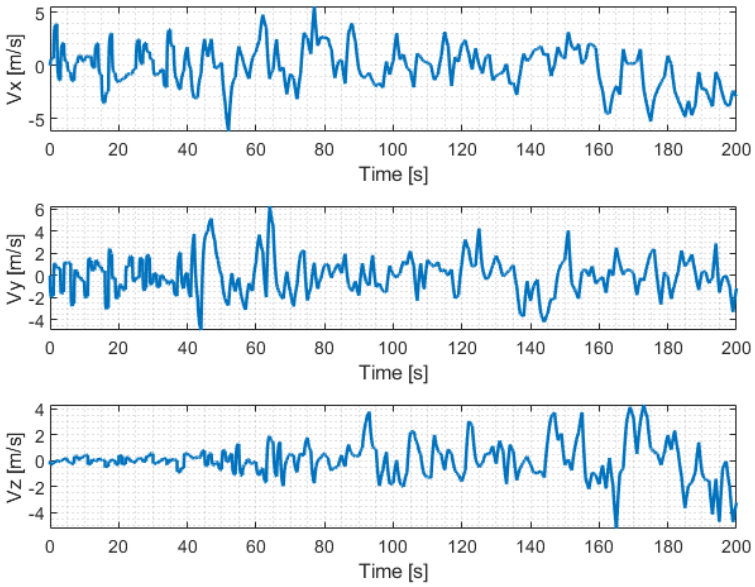

Figure 5.14: Wind linear velocities in body axis

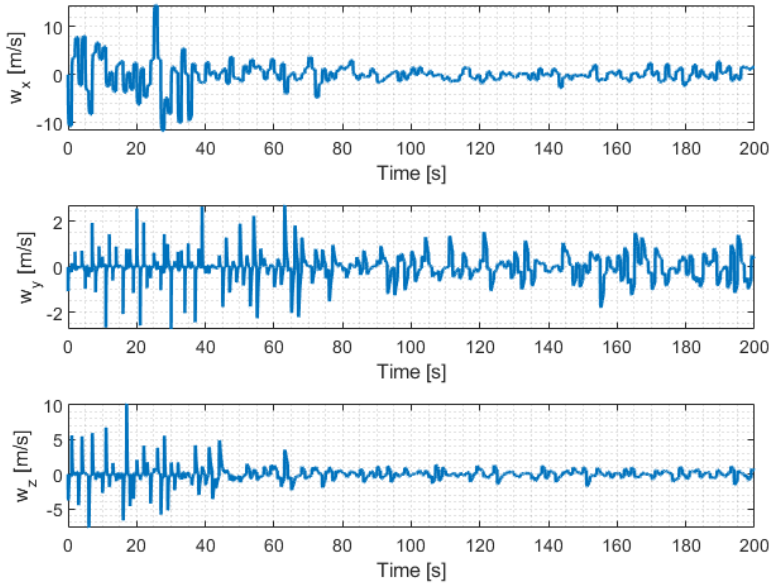

Figure 5.15: Wind angular rates in body axis

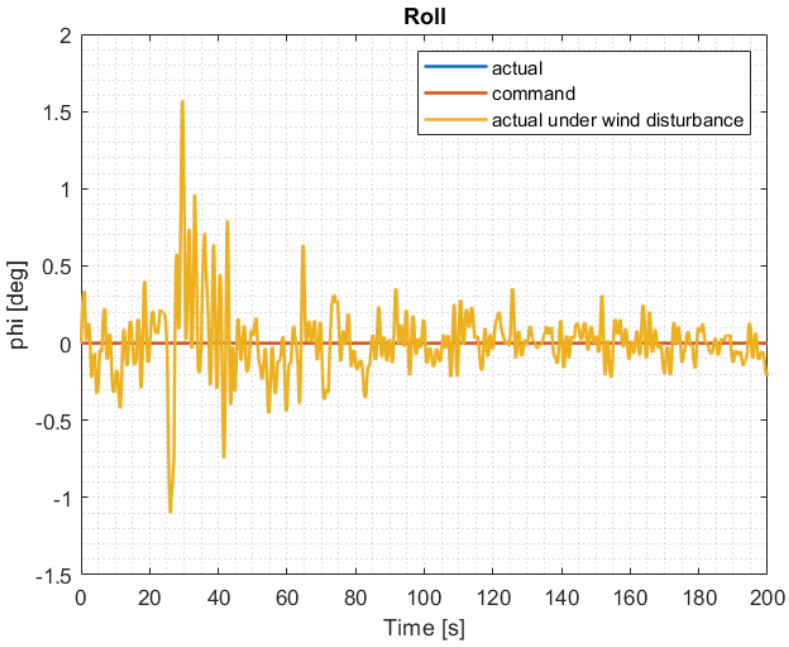

Figure 5.16: Roll attitude using gain-scheduled controller under fixed disturbance

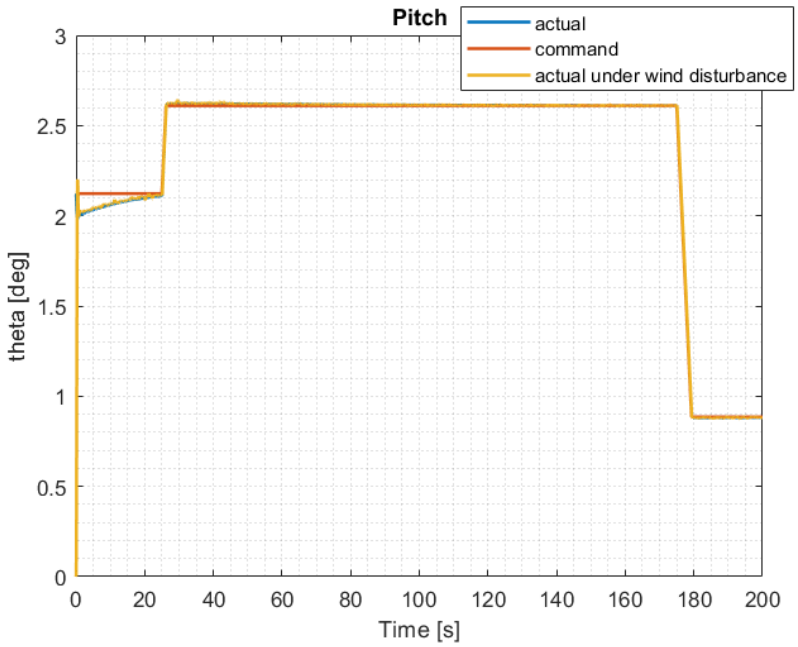

Figure 5.17: Pitch attitude using gain-scheduled controller under fixed disturbance

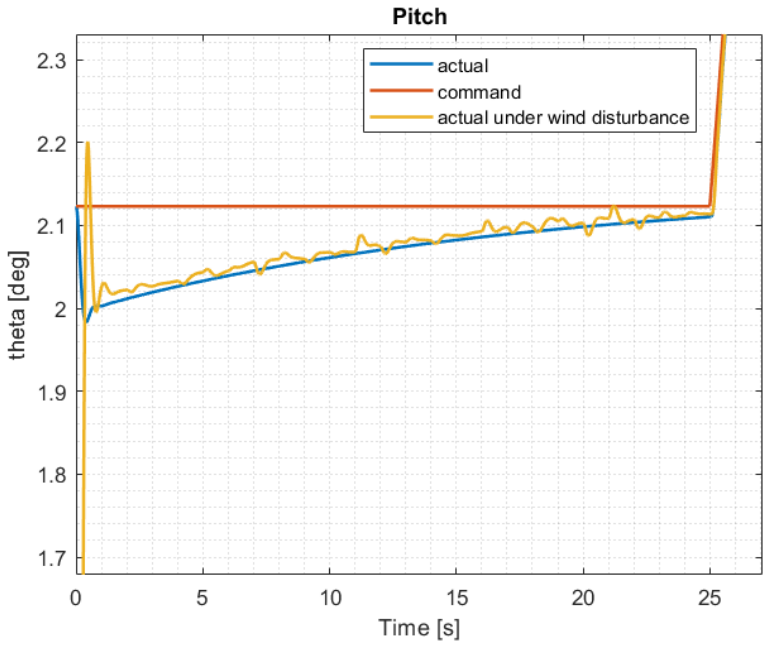

Figure 5.18: Pitch attitude of the first flight stage using gain-scheduled controller under fixed disturbance

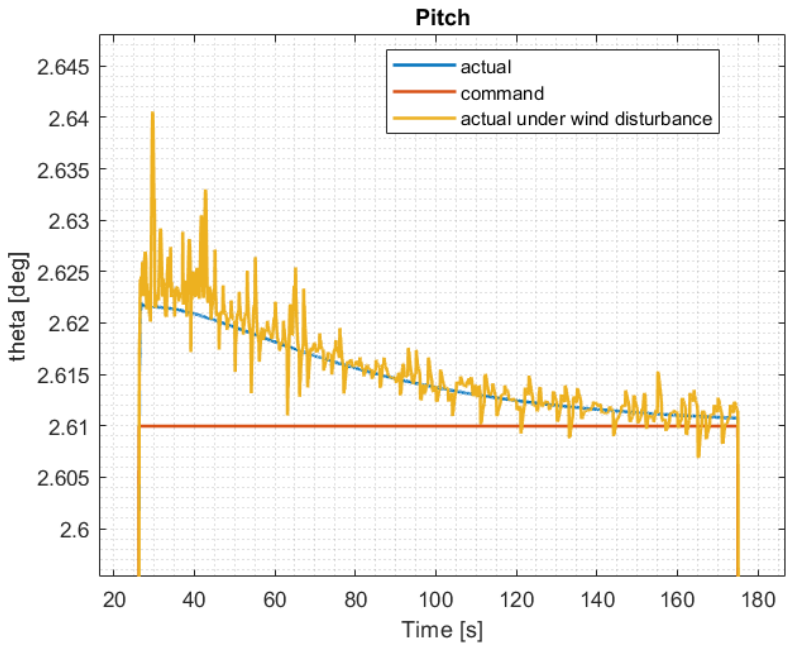

Figure 5.19: Pitch attitude of the second flight stage using gain-scheduled controller under fixed disturbance

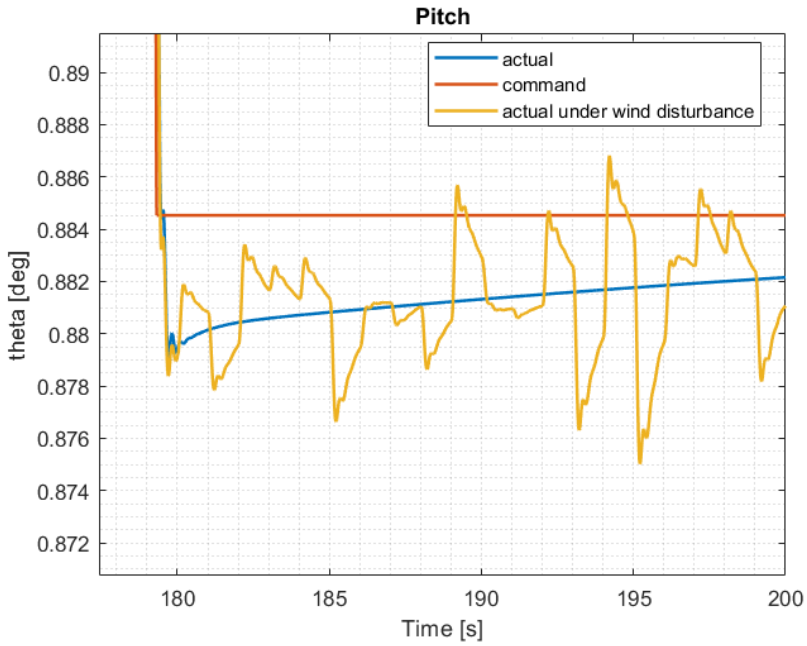

Figure 5.20: Pitch attitude of the third flight stage using gain-scheduled controller under fixed disturbance

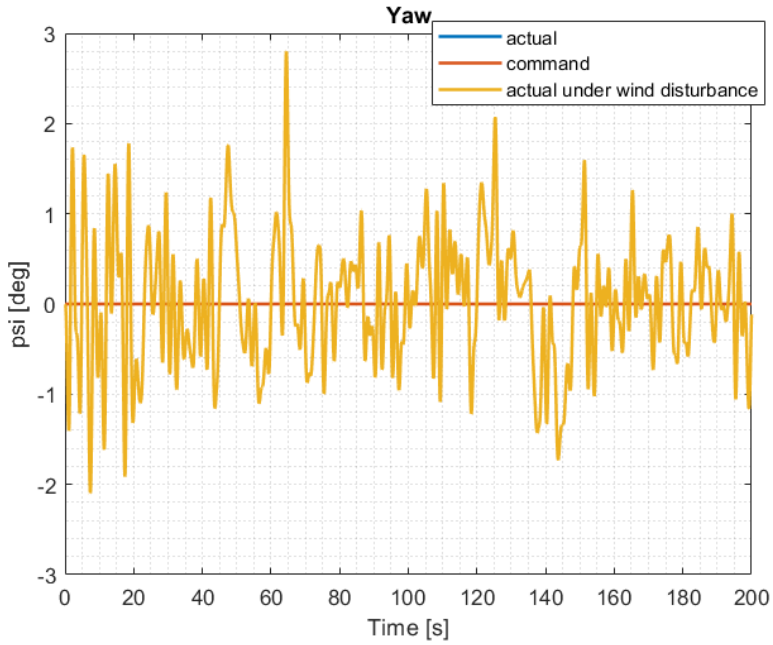

Figure 5.21: Yaw attitude using gain-scheduled controller under fixed disturbance

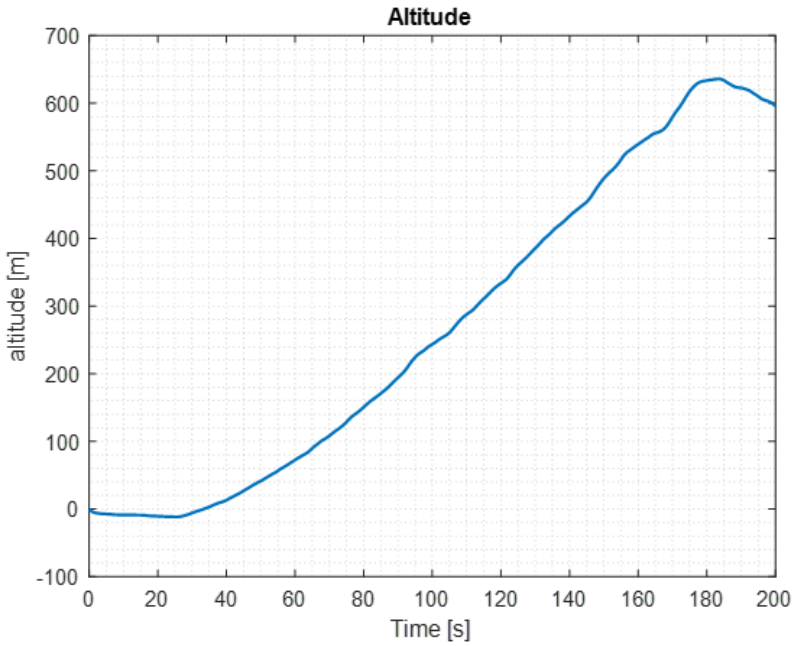

Figure 5.22: Altitude using gain-scheduled controller under fixed disturbance

Upon comparing the results of the gain-scheduled controller following the introduction of wind disturbance with the nominal case, a noticeable decline in the controller's performance becomes evident in the presence of the added disturbance. The most significant errors are

observed in the attitude graphs, particularly the roll and yaw graphs (Figures 5.16 and 5.21). In these graphs, the nominal case's actual values, which are nearly zero, are included. However, they are not apparent due to the substantial errors seen in both roll and yaw attitudes following the introduction of wind disturbance.

Analyzing the altitude graph (Figure 5.22) reveals that the aircraft struggles to maintain steady-level flight post the introduction of wind disturbance. Examining the pitch graphs (Figures 5.17 -5.20) shows an increase in error after the addition of wind disturbance, albeit the error in pitch is comparatively smaller than the errors observed in roll and yaw attitudes.One possible explanation for this lies in the integration of wind linear velocities into the aerodynamic model. Specifically, the Vx velocity is used in calculating Drag force, Vy for Sideslip force, and Vz for Lift force. Upon comparing the magnitudes of these three aerodynamic forces, it becomes apparent that both Drag and Lift forces have significantly bigger magnitudes compared to the Sideslip force. Consequently, the impact of the disturbance is more obvious along the X and Z axes compared to the Y axis.

5.5 DOBC Based on Gain-Scheduled Controller

Following the incorporation of wind disturbance into the gain-scheduled controller, a linear disturbance observer is introduced to estimate and subsequently cancel the total disturbance in the system. The disturbance observer's estimation encompasses not only the wind disturbance but also incorporates non-linearities within the system and uncertainties associated with the parameters used in the model.

For this simulation, a different approach is used to incorporate the wind disturbance. Instead of adding the wind velocities to the aircraft velocity inputs in the aerodynamic model, a duplicate aerodynamic model is created. This duplicate model excludes the control surfaces effects (δa, δe, and δr) from the aerodynamic model. The outputs of this second aerodynamic model are the wind forces and moments which are added as disturbance to the disturbance observer, along with the system nonlinearities.

5.5.1 Disturbance Estimation

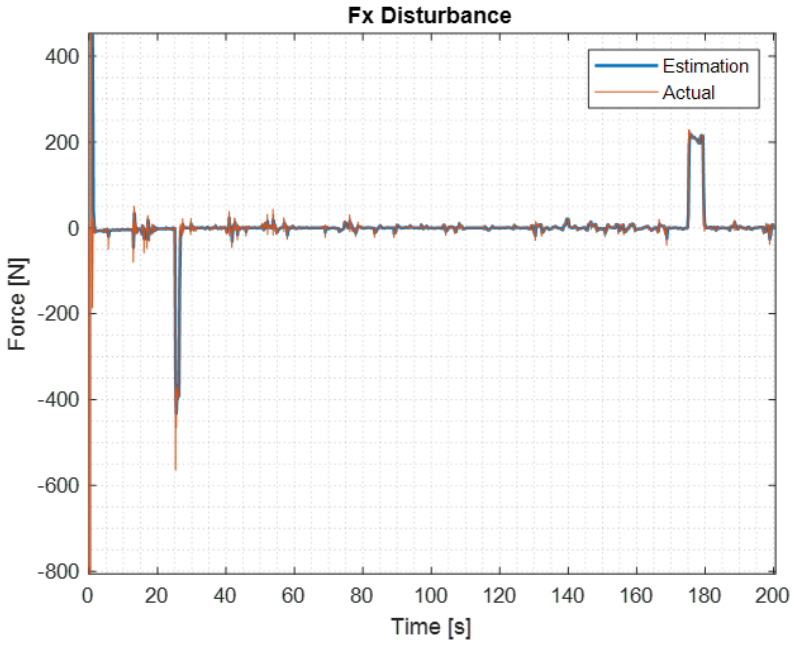

Figure 5.23: Total vs estimated disturbance force along the aircraft's body X-axis

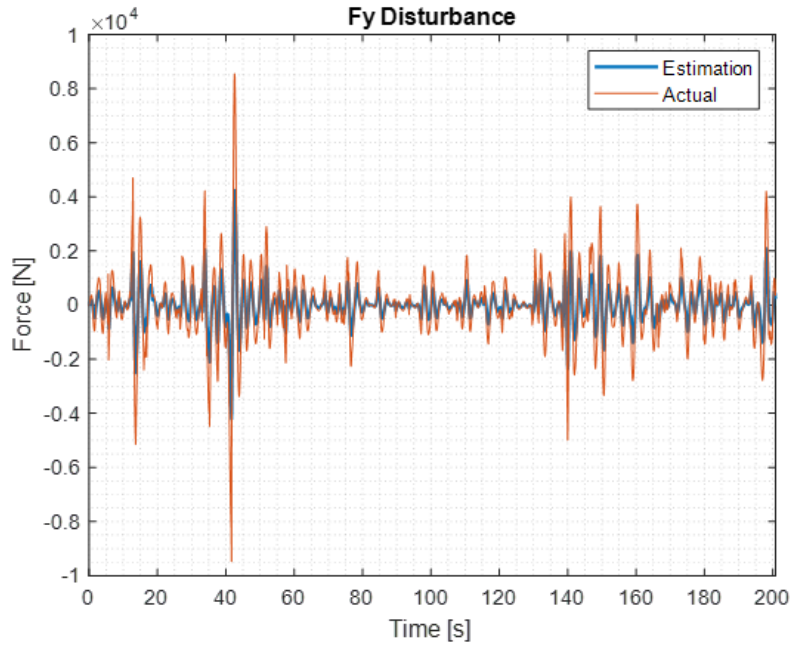

Figure 5.24: Total vs estimated disturbance force along the aircraft's body Y-axis

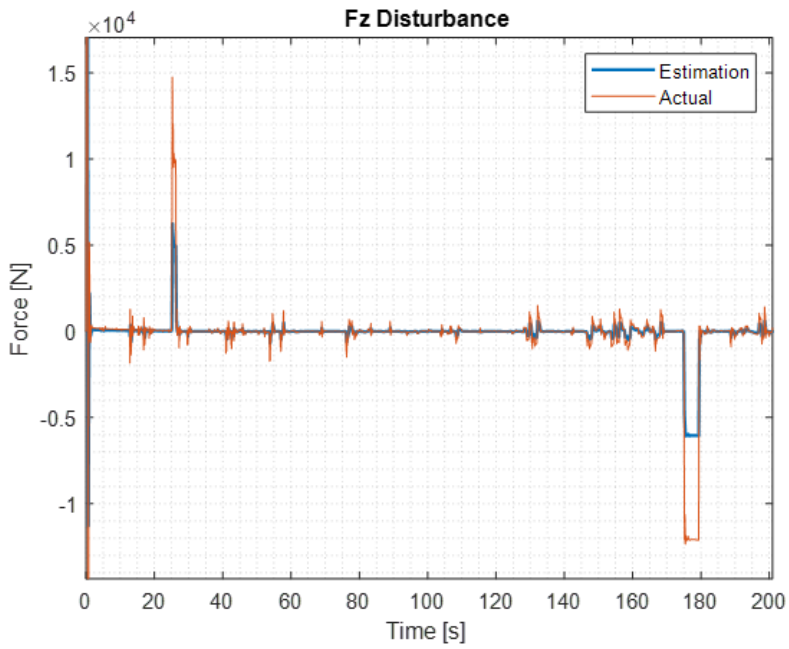

Figure 5.25: Total vs estimated disturbance force along the aircraft's body Z-axis

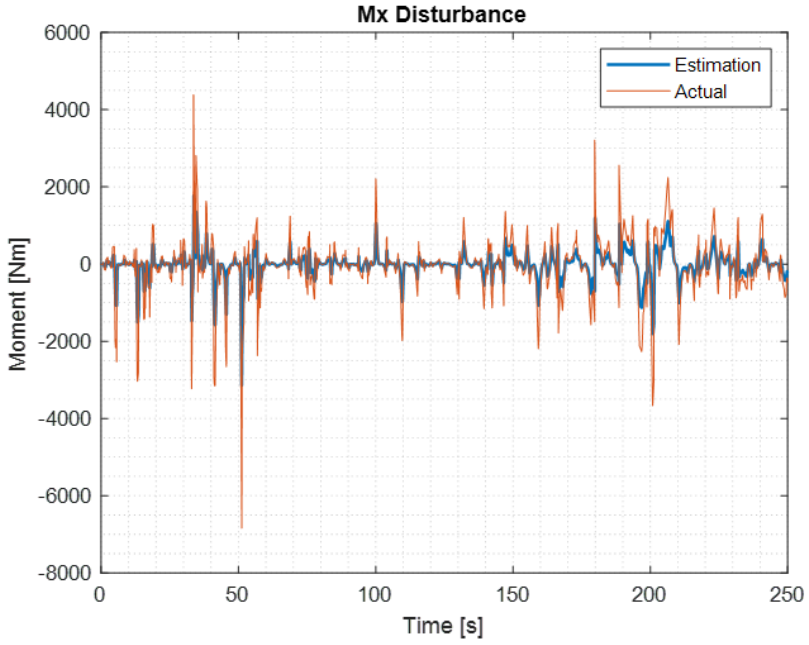

Figure 5.26: Total vs estimated disturbance moment around the aircraft's body X-axis

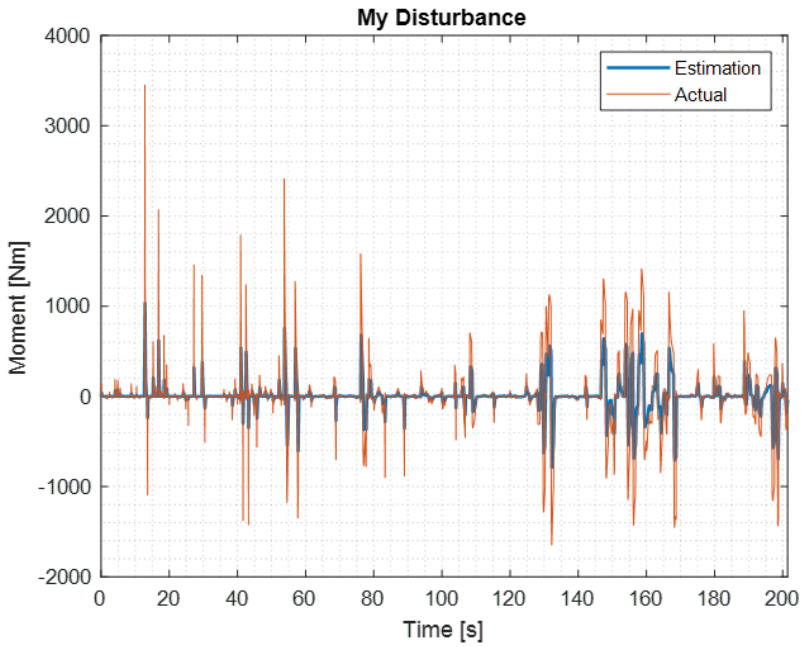

Figure 5.27: Total vs estimated disturbance moment around the aircraft's body Y-axis

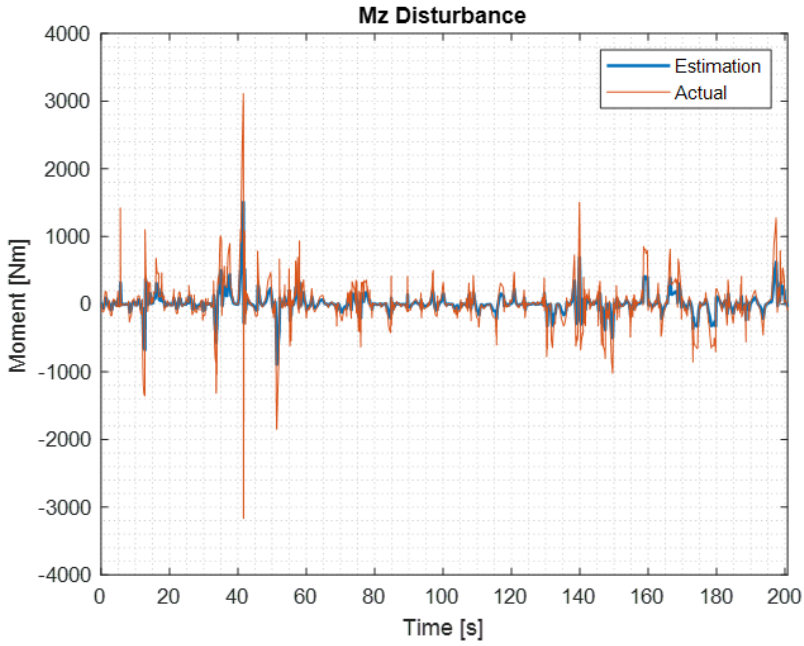

Figure 5.28: Total vs estimated disturbance moment around the aircraft's body Z-axis

Examining the total disturbance against the disturbance estimated by the disturbance observer shows that the disturbance observer provides a good estimation of the total disturbance. Additionally, it can be observed that there are some irregularities for both Fx and Fz disturbances,

occurring during transitions between flight stages. These irregularities take place at the same time when when the flight stage changes. As flight stage changes, there are also changes in the aircraft's angular velocities, with the most significant impact observed in the pitch angular velocity (q). As pitch angular velocity affects velocity and force calculations in the X and Z axes, the effects are mainly seen in the Fx and Fz graphs.

5.5.2 Controller Results

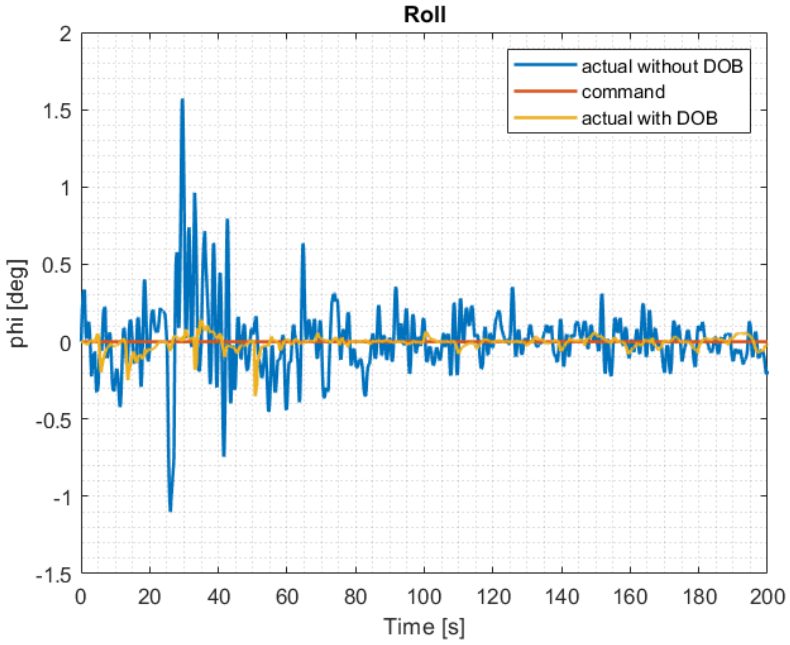

Figure 5.29: Roll attitude using DOBC under wind disturbance

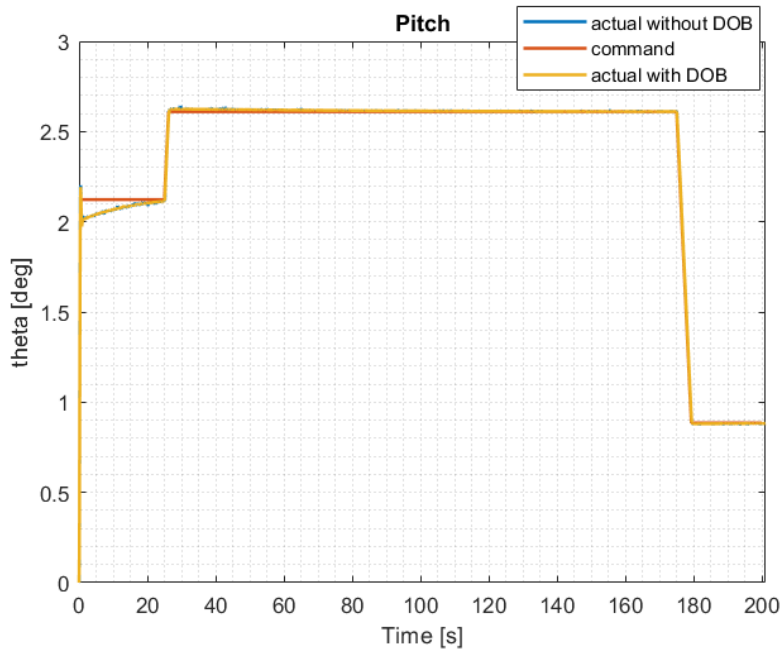

Figure 5.30: Pitch attitude using DOBC under wind disturbance

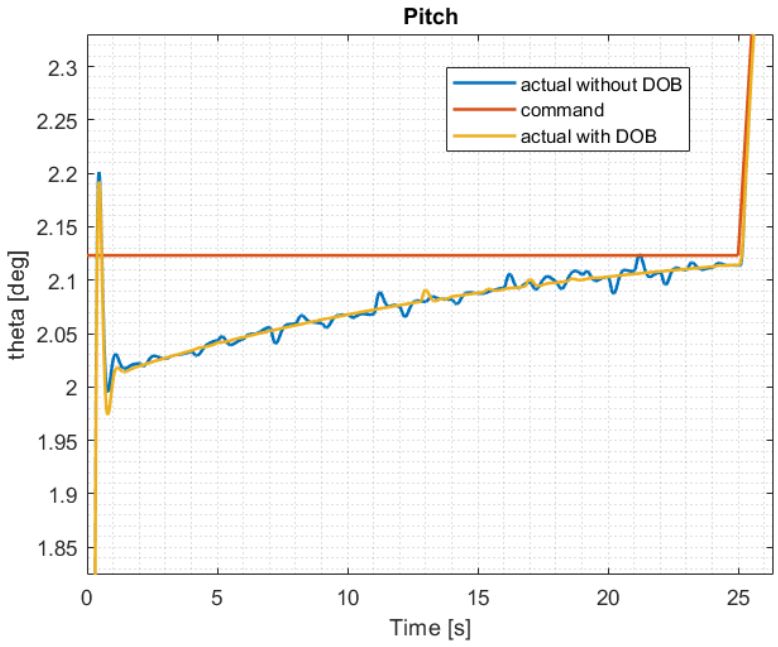

Figure 5.31: Pitch attitude of the first flight stage using DOBC under wind disturbance

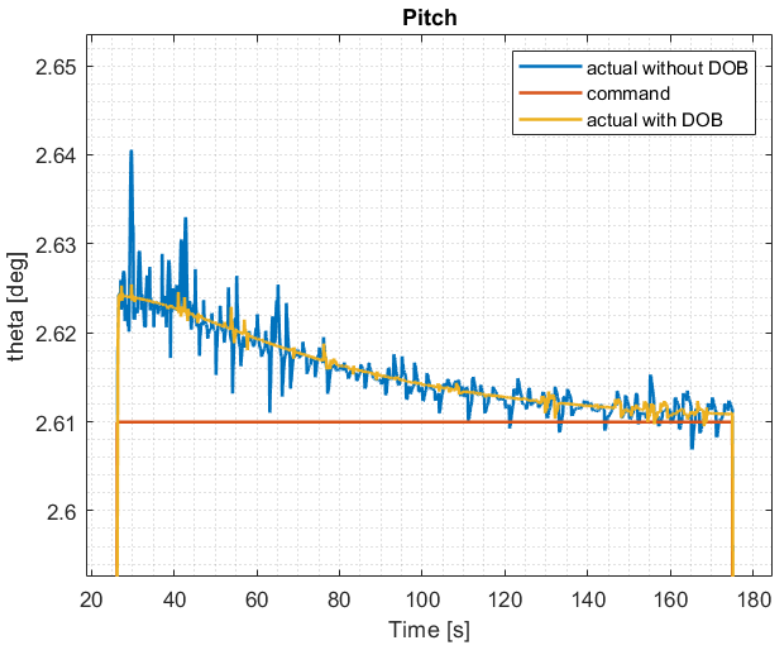

Figure 5.32: Pitch attitude of the second flight stage using DOBC under wind disturbance

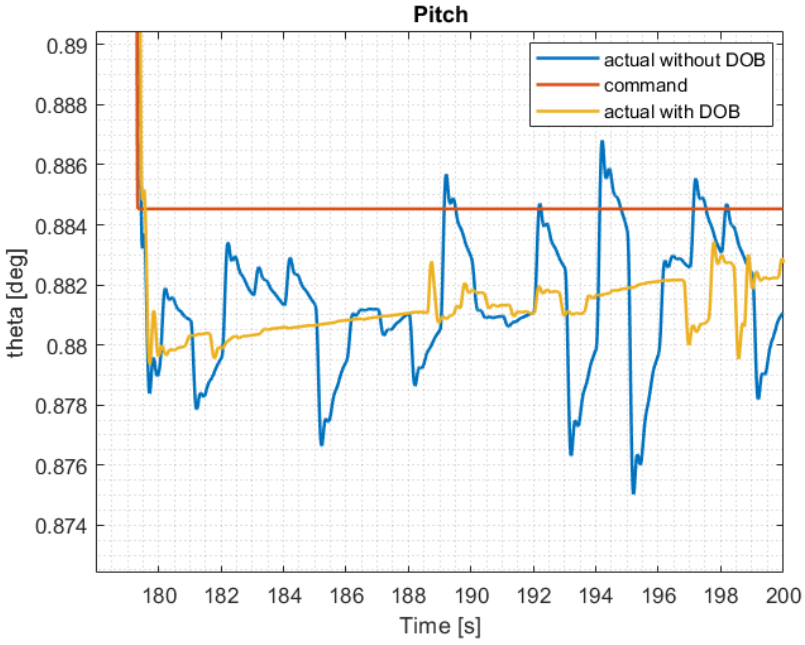

Figure 5.33: Pitch attitude of the third flight stage using DOBC under wind disturbance

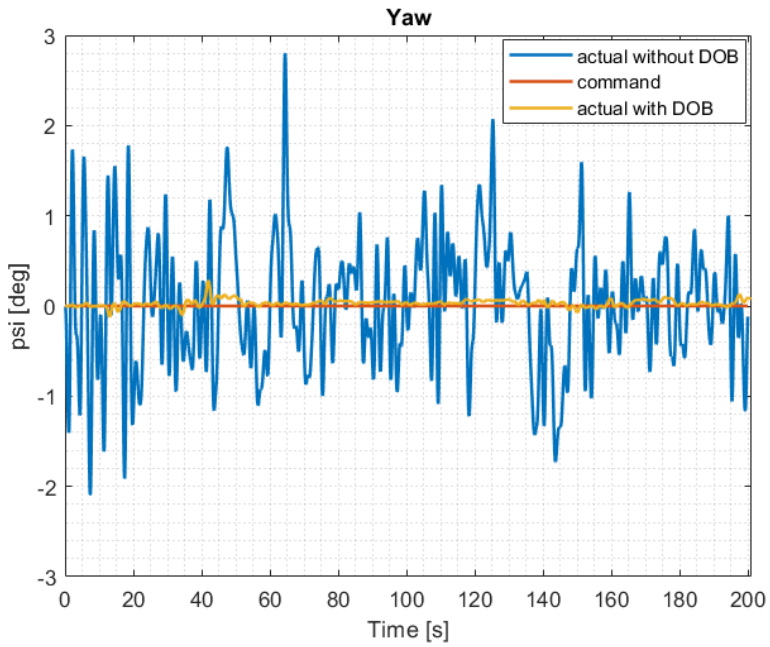

Figure 5.34: Yaw attitude using DOBC under wind disturbance

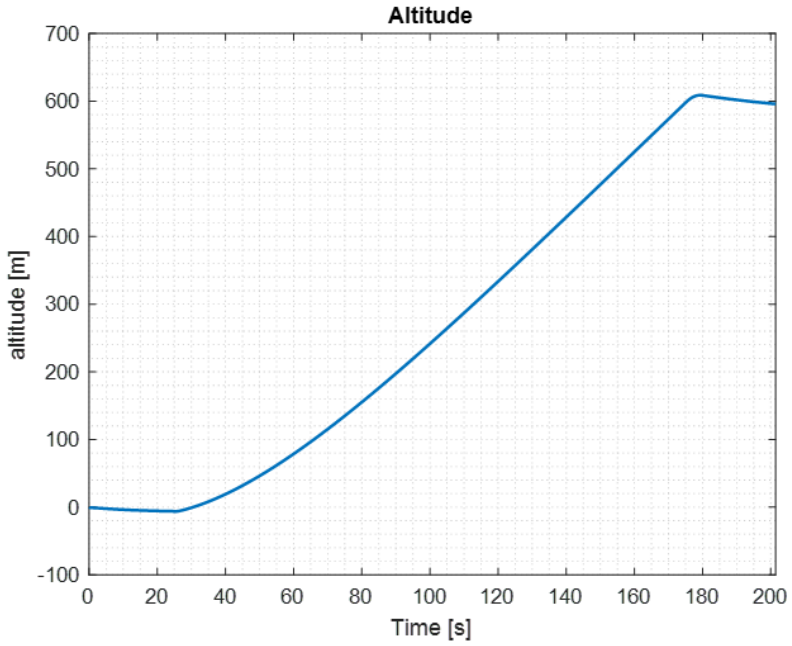

Figure 5.35: Altitude using DOBC under wind disturbance

Comparing the outcomes of the gain-scheduled controller following the introduction of wind disturbance with those of the disturbance observer-based controller reveals a substantial enhancement in the aircraft's performance when disturbances are present. Notably, the error

between the actual and commanded values significantly diminishes for both roll and yaw. Simultaneously, in the case of pitch attitude, a comparison with the previous pitch attitude in the presence of wind disturbance highlights the effective cancellation of the disturbance by the disturbance observer, resulting in remarkably improved results.

Tables 5.9-5.13 illustrate the minimum, maximum, and root-mean-squared errors corresponding to the roll, pitch, yaw outputs.

Controller	RMSE	$\|E_{min}\|$	$\|E_{max}\|$
DOB+GS	0.026	0	0.1575
GS	0.2204	0	1.5715

Table 5.9: Roll attitude errors for DOB+GS

Controller	RMSE	$\|E_{min}\|$	$\|E_{max}\|$
DOB+GS	0.0522	0.0089	0.1020
GS	0.0549	5.2068e-06	0.1060

Table 5.10: First flight stage pitch attitude errors for DOB+GS

Controller	RMSE	$\|E_{min}\|$	$\|E_{max}\|$
DOB+GS	0.0070	8.5979e-07	0.0155
GS	0.0074	3.4410e-07	0.0349

Table 5.11: Second flight stage pitch attitude errors for DOB+GS

Controller	RMSE	$\|E_{min}\|$	$\|E_{max}\|$
DOB+GS	0.0021	1.4801e-05	0.0050
GS	0.0039	3.5850e-07	0.0095

Table 5.12: Third flight stage pitch attitude errors for DOB+GS

Controller	*RMSE*	$\|E_{min}\|$	$\|E_{max}\|$
DOB+GS	0.0537	0	0.2823
GS	2.4103	0	2.6406

Table 5.13: Yaw attitude errors for DOB+GS

5.6 Conditional Integral Sliding Mode Controller (C-ISMC)

Following simulations with the gain-scheduled controller, a different controller is evaluated to improve the robustness of the autopilot's control architecture. In this simulation, the Conditional Integral Sliding Mode Controller (C-ISMC) is applied without introducing any disturbances. The purpose of this simulation is to assess the performance of the C-ISMC and compare its results with the nominal scenario of the gain-scheduled controller in the absence of disturbances.

It is important to emphasize that the C-ISMC exclusively addresses the longitudinal dynamics of the aircraft. Specifically, the controller's output in this context is the elevator command. Meanwhile, the existing cascaded gain-scheduled controller structure is maintained for the lateral dynamics. Consequently, the examination of the C-ISMC is limited to the longitudinal dynamics of the aircraft.

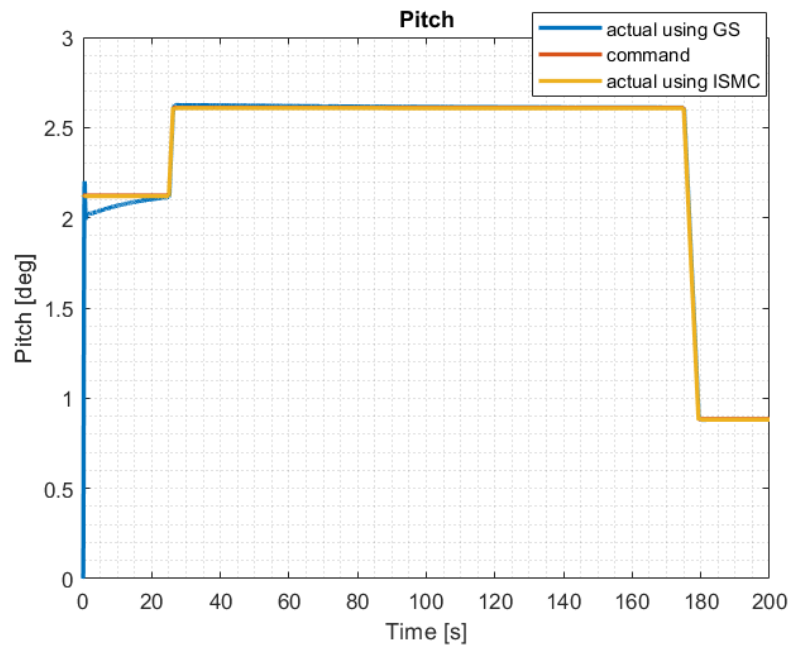

Figure 5.36: Pitch attitude using C-ISMC

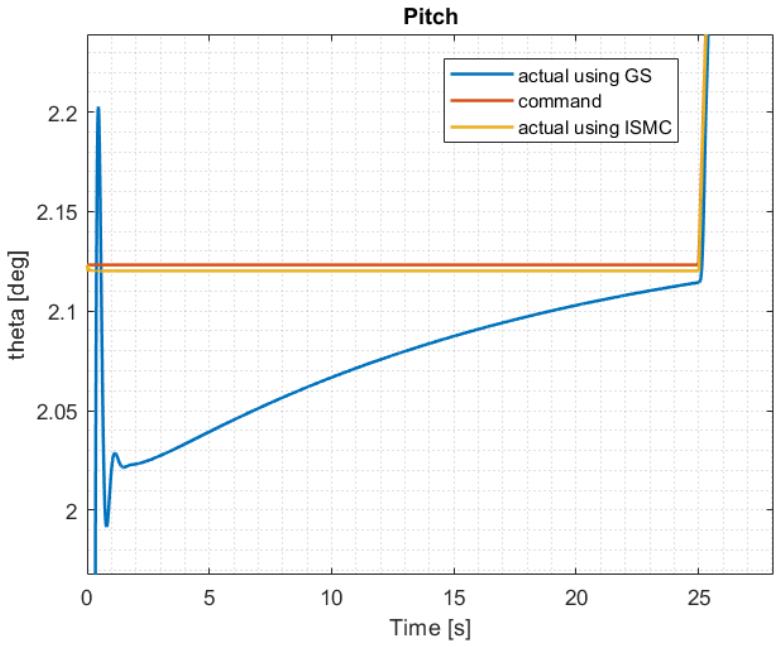

Figure 5.37: Pitch attitude of the first flight stage using C-ISMC

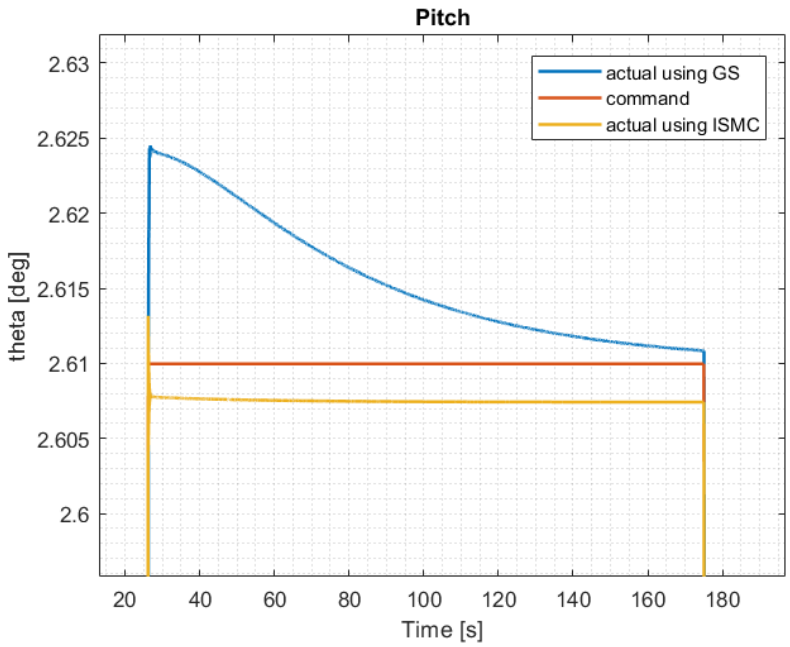

Figure 5.38: Pitch attitude of the second flight stage using C-ISMC

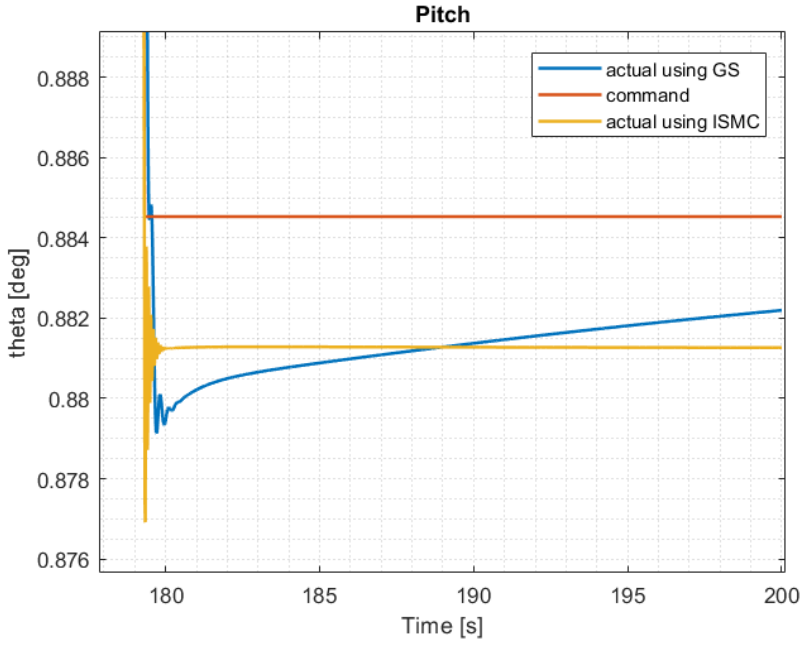

Figure 5.39: Pitch attitude of the third flight stage using C-ISMC

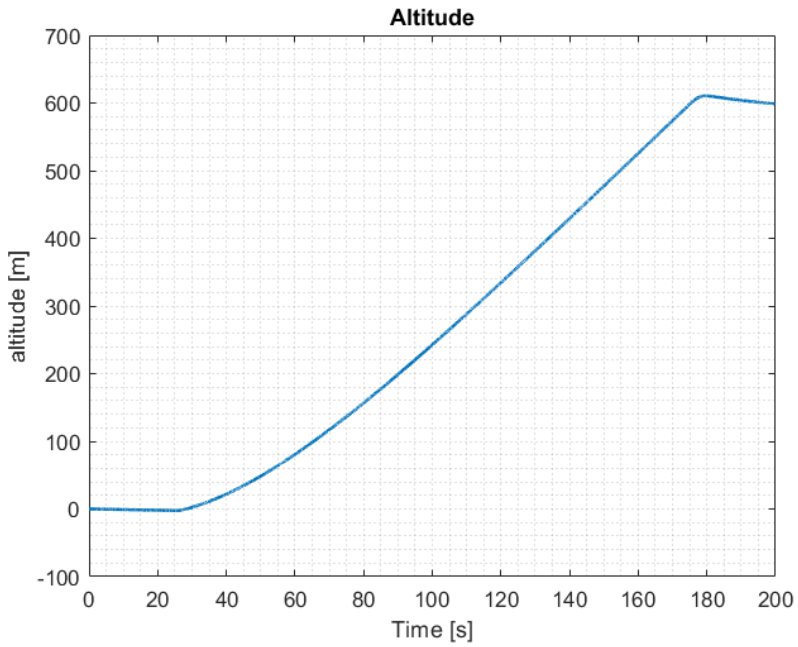

Figure 5.40: Altitude using C-ISMC

Tables 5.14-5.16 show the errors of the pitch attitude for the different flight stages of both the gain-scheduled and C-ISMC controllers.

Controller	RMSE	$\|E_{min}\|$	$\|E_{max}\|$
GS	0.0581	0.0129	0.1099
C-ISMC	0.003	0.003	0.003

Table 5.14: First flight stage pitch attitude errors for C-ISMC

Controller	RMSE	$\|E_{min}\|$	$\|E_{max}\|$
GS	0.0060	7.8734e-04	0.0120
C-ISMC	0.0025	5.1786e-04	0.004

Table 5.15: Second flight stage pitch attitude errors for C-ISMC

Controller	RMSE	$\lvert E_{min} \rvert$	$\lvert E_{max} \rvert$
GS	0.0033	0.0024	0.0049
C-ISMC	0.0033	0.0033	0.0032

Table 5.16: Third flight stage pitch attitude errors for C-ISMC

Upon analyzing the graphs and error tables, it becomes evident that the conditional integral sliding mode controller exhibits generally superior performance compared to the gain-scheduled controller. The Root Mean Square Error (RMSE), absolute minimum, and absolute maximum errors for the initial two flight stages all demonstrate improvement with the C-ISMC. While there is a slight improvement in the third flight stage when examining the maximum absolute error, with nearly identical RMSE and absolute minimum errors, it can still be asserted that the performance of the C-ISMC surpasses that of the gain-scheduled controller.

5.7 C-ISMC Under Fixed Disturbance

Following the evaluation of the C-ISMC controller's performance in the absence of disturbance, a fixed disturbance is introduced into the system. Similar to the approach taken with the gain-scheduled controller, the fixed disturbance is added only to the elevator command input derived from the C-ISMC controller. Another logical justification for limiting the disturbance to the elevator input is that the C-ISMC is specifically used for the control of the longitudinal dynamics of the aircraft. Consequently, to assess its robustness against fixed disturbance, the disturbance is applied to the elevator command. The fixed disturbance added for this simulation is 3 degrees added to the elevator command. Similar to the scenario with the gain-scheduled controller under fixed disturbance, a fixed disturbance of 3 degrees is incorporated into the elevator command for this simulation.

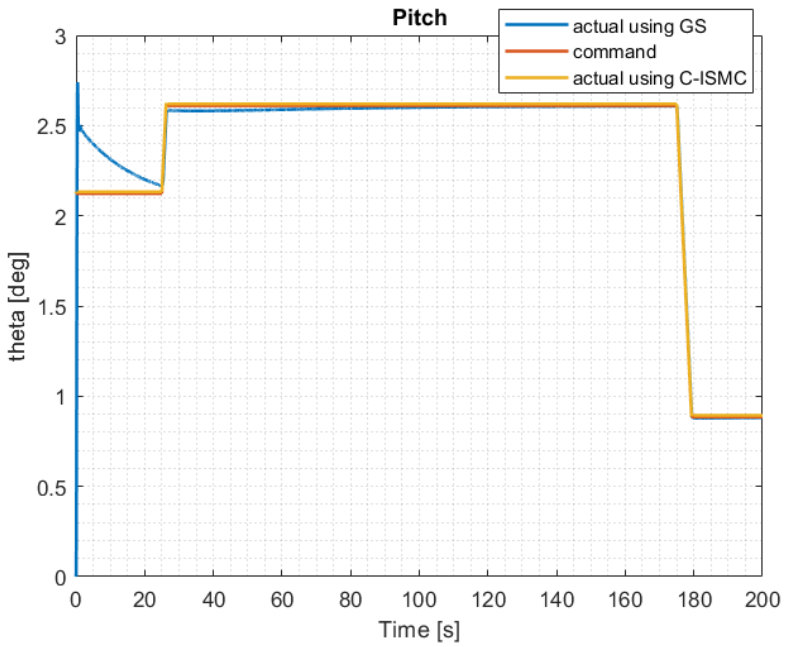

Figure 5.41: Pitch attitude using C-ISMC controller under fixed disturbance

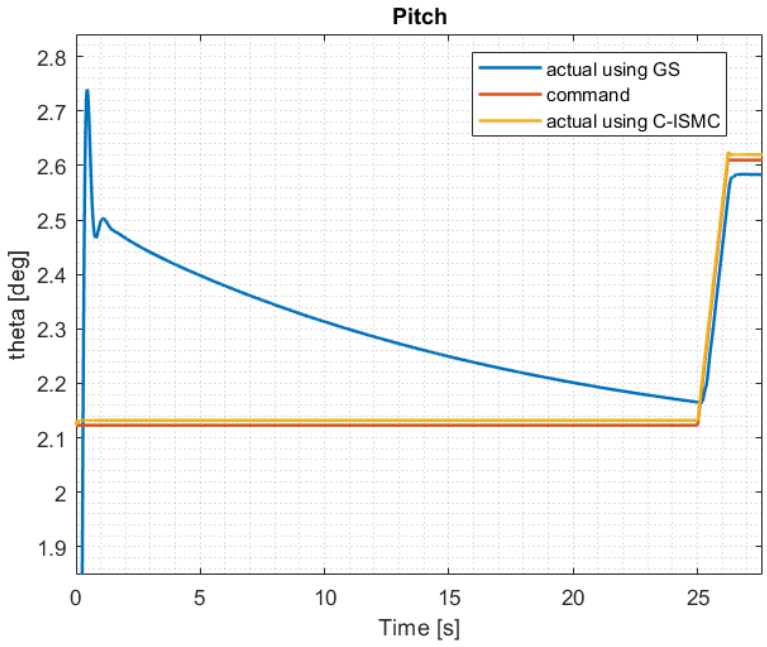

Figure 5.42: Pitch attitude of the first flight stage using C-ISMC controller under fixed disturbance

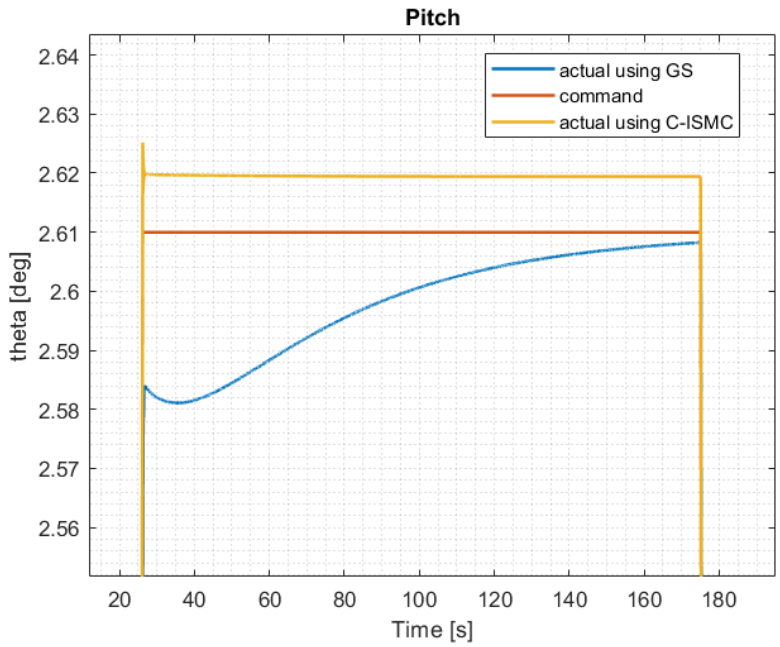

Figure 5.43: Pitch attitude of the second flight stage using C-ISMC controller under fixed disturbance

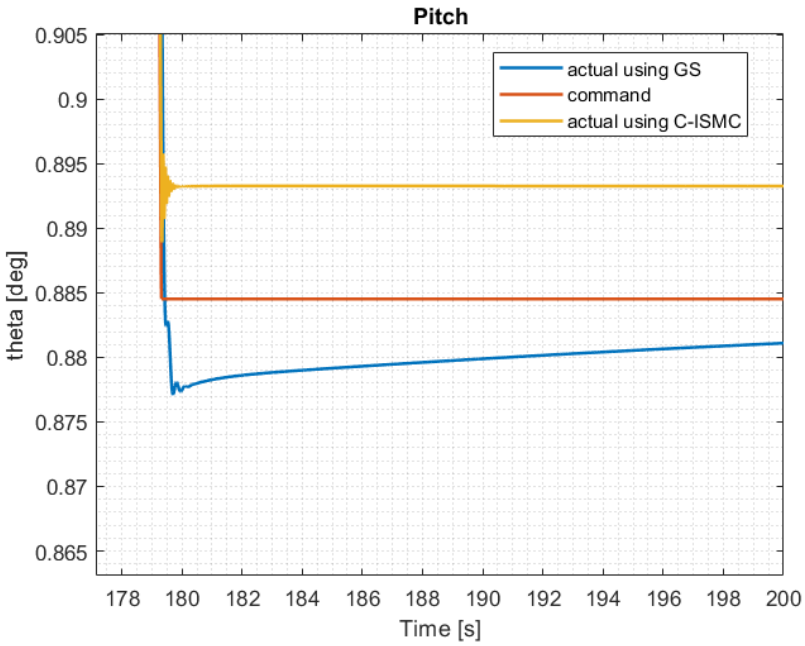

Figure 5.44: Pitch attitude of the third flight stage using C-ISMC controller under fixed disturbance

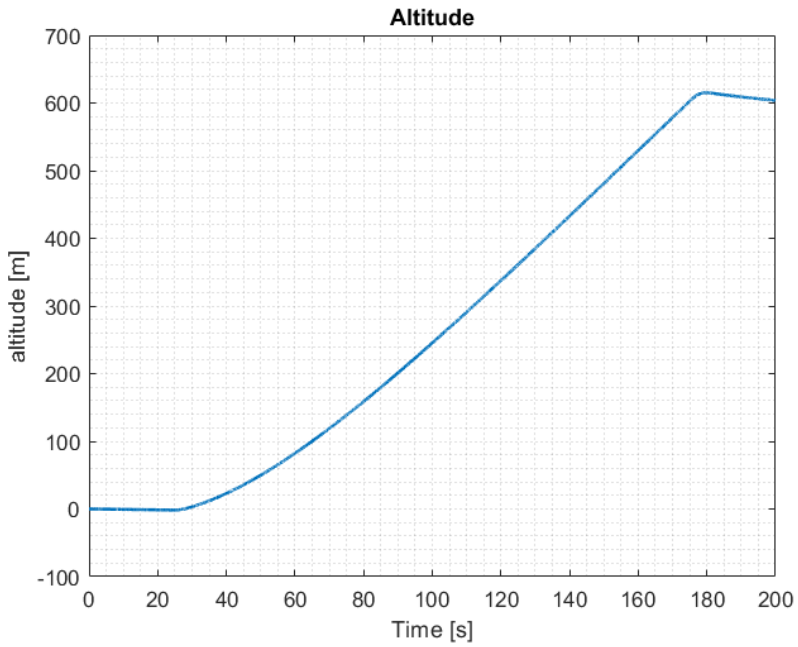

Figure 5.45: Altitude using C-ISMC controller under fixed disturbance

Tables 5.17-5.20 show the errors of the pitch attitude for the different flight stages of both the gain-scheduled and C-ISMC controllers under fixed disturbance.

Controller	RMSE	$\|E_{min}\|$	$\|E_{max}\|$
GS	0.178	0.0423	0.3371
C-ISMC	0.009	0.009	0.009

Table 5.17: First flight stage pitch attitude errors for C-ISMC under fixed disturbance

Controller	RMSE	$\|E_{min}\|$	$\|E_{max}\|$
GS	0.0154	0.0017	0.0354
C-ISMC	0.0095	0.008	0.0128

Table 5.18: Second flight stage pitch attitude errors for C-ISMC under fixed disturbance

Controller	RMSE	$\lvert E_{min} \rvert$	$\lvert E_{max} \rvert$
GS	0.0048	0.0034	0.0068
C-ISMC	0.0087	0.0087	0.0088

Table 5.19: Third flight stage pitch attitude errors for C-ISMC under fixed disturbance

Examining the initial two flight stages (Figures 5.43-5.44) reveals that the C-ISMC exhibits greater robustness compared to the gain-scheduled controller in the presence of a fixed disturbance. Conversely, a small degradation in the performance of the C-ISMC is observed in terms of root mean square error (rmse), absolute minimum, and absolute maximum errors during the last flight stage. However, it is noteworthy that the difference between the error magnitudes for the C-ISMC and the gain-scheduled controller is smaller for the last flight stage than for the first two stages. Moreover, unlike the gain-scheduled controller, which requires time for the integrator to compensate for the fixed disturbance, the C-ISMC instantly shows robustness from the initial flight stage against fixed disturbance. Therefore, because of these two reasons, the overall conclusion remains that throughout the flight envelope, the C-ISMC demonstrates more robust performance in the presence of a fixed disturbance.

Examining the pitch graphs reveals a bias across all flight stages, which is attributed to the methodology employed in implementing the C-ISMC. The approach used in this study utilizes the pitch angular velocity error in the controller design. Instead, a potential remedy for the bias is to directly use the pitch angle error in the design of the C-ISMC. Regarding the altitude graph, there is no apparent change in the aircraft's altitude throughout the flight envelope.

5.8 DOBC Based on C-ISMC

After assessing the robustness of the C-ISMC under fixed disturbance and comparing it with the robustness of the gain-scheduled controller, a novel disturbance observer-based controller is formulated based on C-ISMC. This newly designed controller is then compared with the first disturbance observer-based controller that uses the gain-scheduled controller. The linear

disturbance observer integrated into the C-ISMC is identical to the one integrated into the gain-scheduled controller, featuring an identical first-order low-pass filter with the same cut-off frequency of 10 rad/s. The following subsections present the comprehensive disturbance estimation results for each axis, followed by an analysis of the errors associated with the proposed disturbance observer-based controller.

5.8.1 Disturbance Estimation

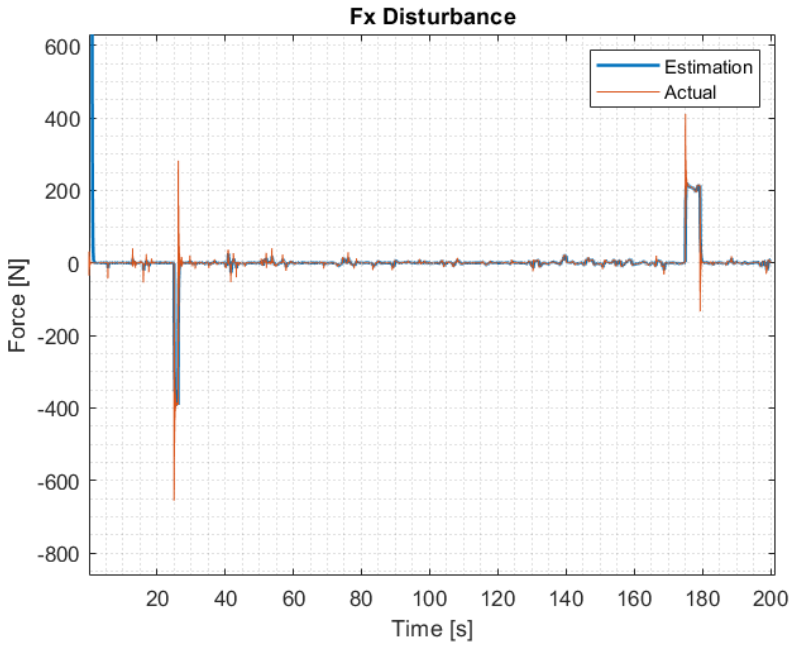

Figure 5.46: Total vs estimated disturbance force along the aircraft's body X-axis using C-ISMC

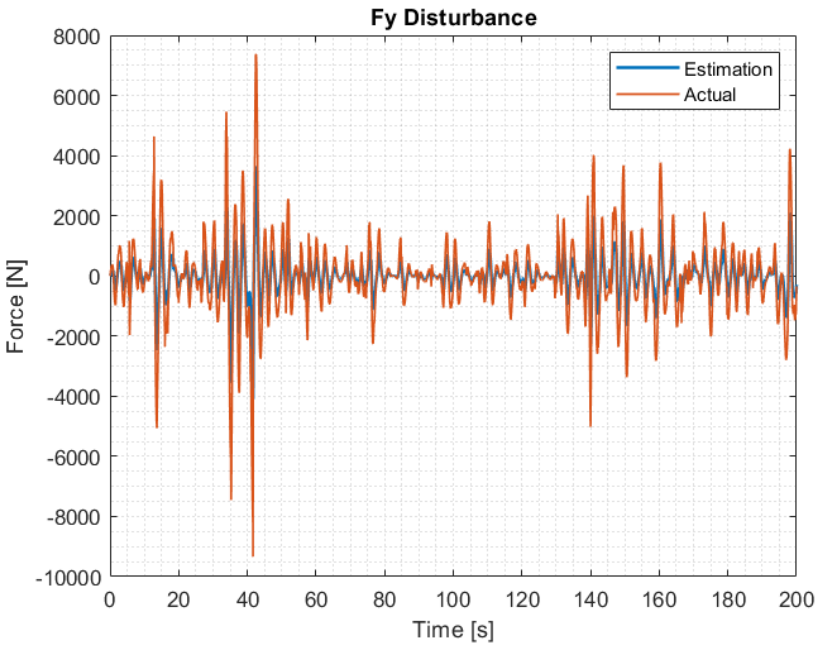

Figure 5.47: Total vs estimated disturbance force along the aircraft's body Y-axis using C-ISMC

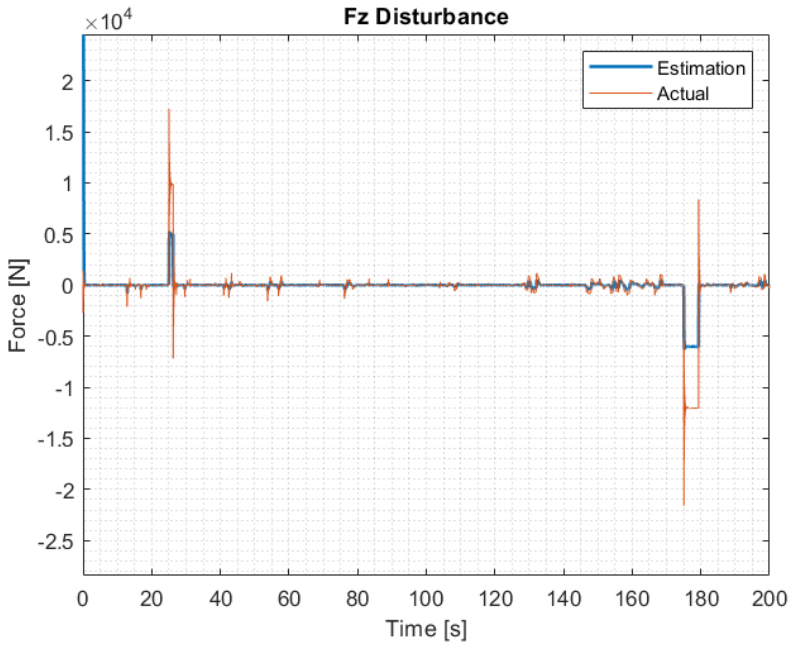

Figure 5.48: Total vs estimated disturbance force along the aircraft's body Z-axis using C-ISMC

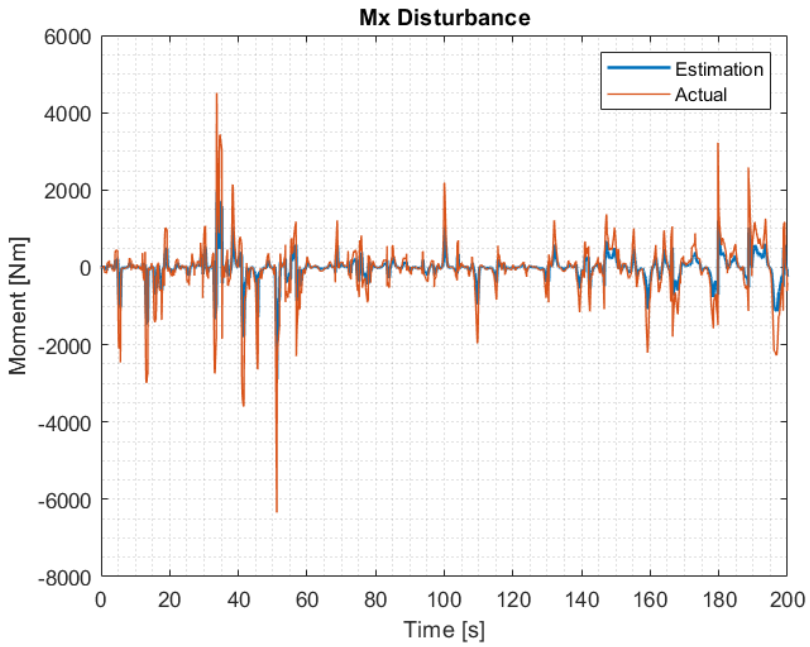

Figure 5.49: Total vs estimated disturbance moment around the aircraft's body X-axis using C-ISMC

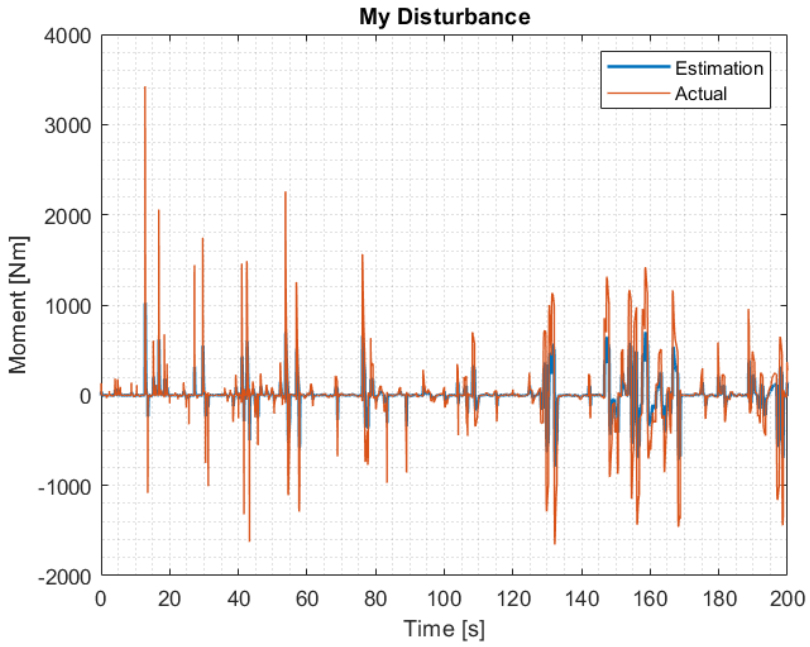

Figure 5.50: Total vs estimated disturbance moment around the aircraft's body Y-axis using C-ISMC

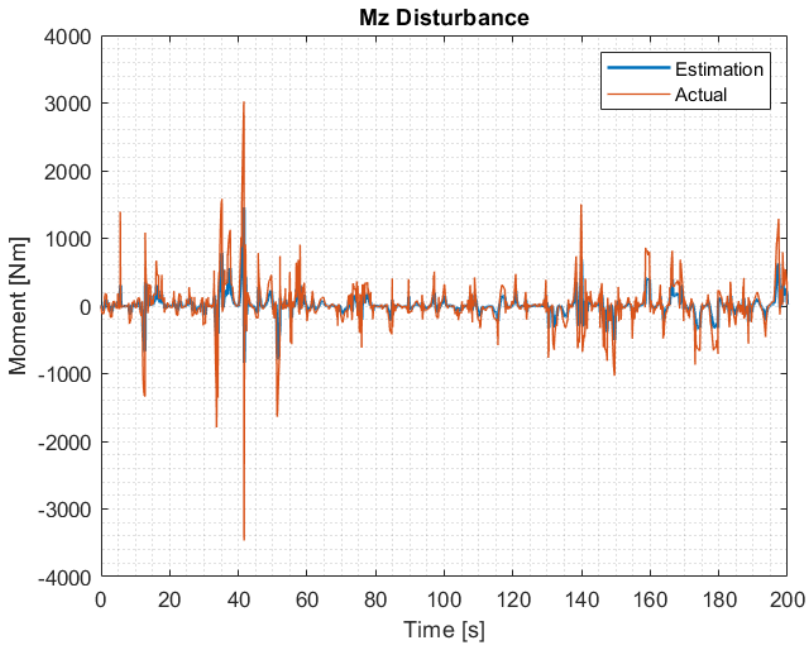

Figure 5.51: Total vs estimated disturbance moment around the aircraft's body Z-axis using C-ISMC

Upon examining Figures 5.46-5.51, it is evident that the disturbance estimation performance achieved for the DOBC with the C-ISMC is similar compared to that of the DOBC based on the gain-scheduled controller.

5.8.2 Controller Results

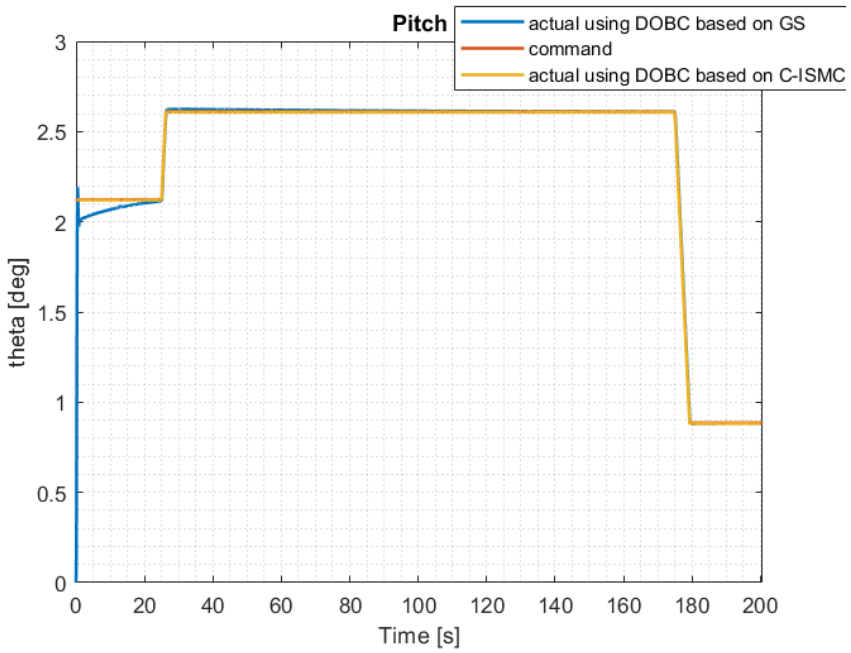

Figure 5.52: Pitch attitude comparison of the two DOBCs

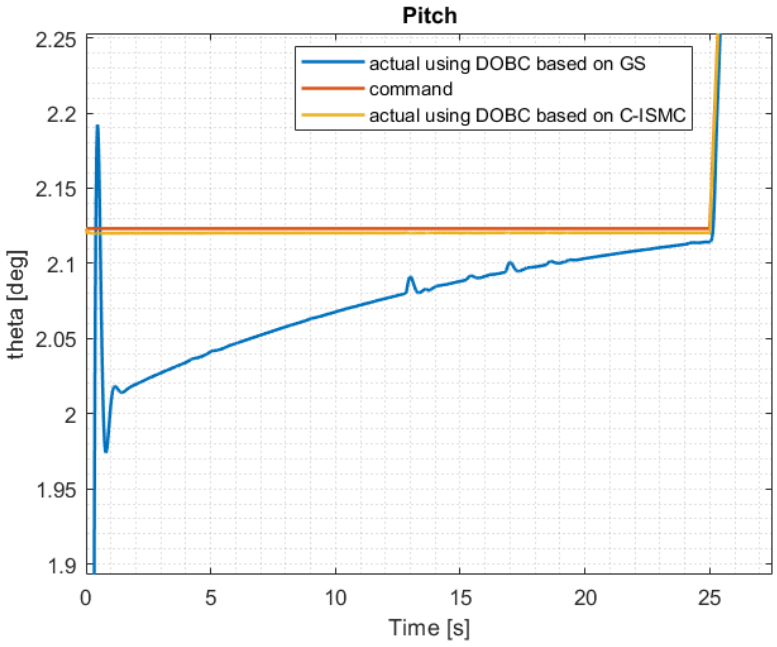

Figure 5.53: Pitch attitude comparison of the two DOBCs for first flight stage

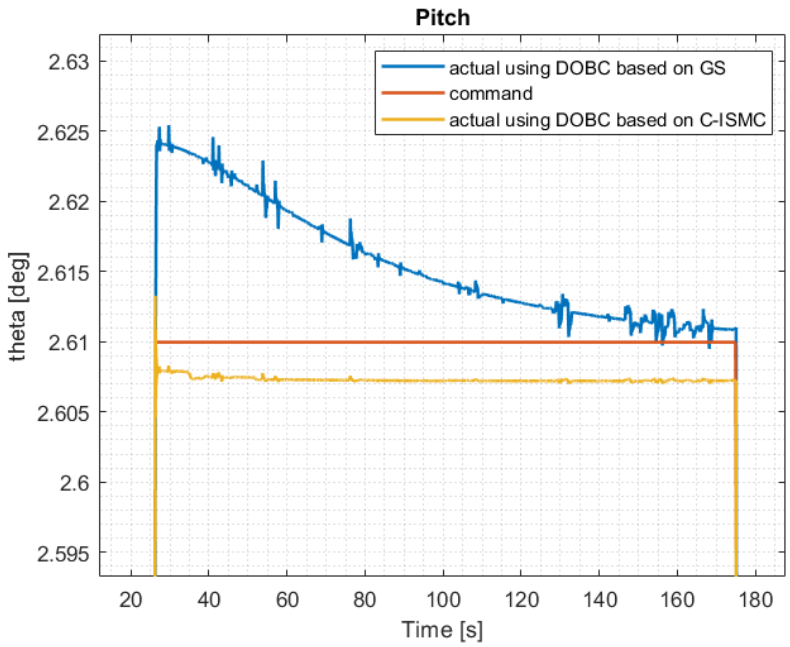

Figure 5.54: Pitch attitude comparison of the two DOBCs for second flight stage

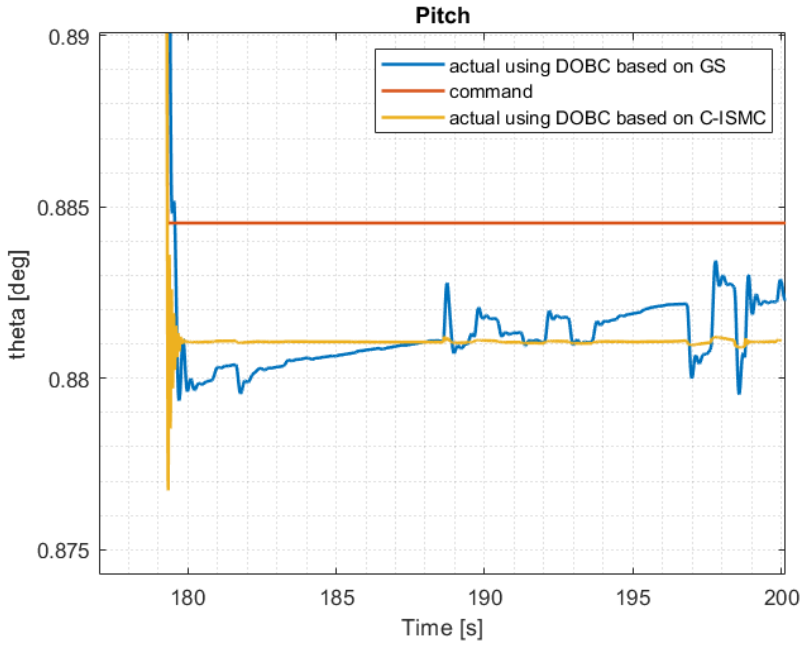

Figure 5.55: Pitch attitude comparison of the two DOBCs for third flight stage

Tables 5.20-5.22 present the pitch attitude errors under wind disturbance for various flight stages, comparing the two distinct disturbance observer-based controllers applied in this study: one based on the gain-scheduled controller and the other based on C-ISMC.

DOBC	RMSE	$\|E_{min}\|$	$\|E_{max}\|$
DOB+GS	0.0522	0.0089	0.1020
DOB+C-ISMC	0.0029	0.0022	0.0032

Table 5.20: First flight stage pitch attitude errors for DOB+C-ISMC

DOBC	RMSE	$\|E_{min}\|$	$\|E_{max}\|$
DOB+GS	0.0070	8.5979e-07	0.0155
DOB+C-ISMC	0.0027	4.2762e-04	0.0039

Table 5.21: Second flight stage pitch attitude errors for DOB+C-ISMC

DOBC	RMSE	$\|E_{min}\|$	$\|E_{max}\|$
DOB+GS	0.0021	0.0033	0.0050
DOB+C-ISMC	0.0035	0.0087	0.0036

Table 5.22: Third flight stage pitch attitude errors for DOB+C-ISMC

Analyzing the first two flight stages shows that the DOBC derived from C-ISMC displays superior robustness in the presence of wind disturbance compared to the DOBC based on the gain-scheduled controller. Conversely, the DOBC based on the gain-scheduled controller exhibits lower Root Mean Square Error (RMSE) and minimum error. However, it is important to note that the discrepancy in error magnitudes between both DOBCs is of a low signifcance in the last flight stage compared to the first two stages. Also, the DOBC based on gain-scheduling takes time for the integrator to compensate for the fixed disturbance. In contrast, the DOBC based on C-ISMC immediately compensates for the fixed disturbance introduced. Consequently, the overall conclusion persists that across the entire flight envelope, the DOBC based on C-ISMC demonstrates more robust performance.

CHAPTER 6

CONCLUSION AND FUTURE WORKS

This thesis explores the design of robust controllers for a fixed-wing UAV based on active disturbance cancellation. The primary goal is to stabilize the pitch attitude and achieve desired performance for both longitudinal and lateral dynamics of the aircraft. The approach involves implementing a gain-scheduled controller based on Proportional-Integral-Derivative (PID) control, with controller parameters tuned for three different trim points of the UAV. These trim points correspond to distinct flight stages in the simulation, including steady-level flight at sea level, a pull-up, and another steady-level flight at an altitude of 600 m. Simulation results validate the effectiveness of the designed gain-scheduled controller. Additional simulations were made under fixed disturbance and wind disturbance, which revealed the controller's performance degradation in the presence of both kinds of disturbance. To address this, a linear disturbance observer is introduced to the controller, enhancing its robustness through active disturbance cancellation, which is achieved by estimating the total disturbance. Simulation results for the Disturbance Observer-Based Controller (DOBC) utilizing the gain-scheduled controller demonstrate an improvement in robustness after the inclusion of the disturbance observer. Subsequently, a Conditional Integral Sliding Mode Controller (C-ISMC) is developed based on the pitch angular rate error. Simulation results indicate that, in both nominal and fixed disturbance cases, the C-ISMC exhibits greater robustness com-

pared to the gain-scheduled controller. This is followed by the integration of a disturbance observer, identical to the one used for the gain-scheduled controller, into the C-ISMC. Simulation outcomes reveal that the DOBC based on C-ISMC surpasses the DOBC based on the gain-scheduled controller in terms of robustness.

As a future work, the C-ISMC approach can be designed based on the pitch attitude error instead of the pitch angular rate error.

Bibliography

[1] Yeonsik Kang and J. Karl Hedrick. “Linear Tracking for a Fixed-Wing UAV Using Nonlinear Model Predictive Control”. In: *IEEE Transactions on Control Systems Technology* 17.5 (Sept. 2009).

[2] Christoforos Kanellakis and George Nikolakopoulos. “Survey on computer vision for UAVs: Current developments and trends”. In: *Journal of Intelligent & Robotic Systems* (2017).

[3] Barak J. Carlson. “Past UAV Program Failures and Implications for Current UAV Programs”. In: *Air University* (2001).

[4] Anna Prach. “Robust Controller Design for a Fixed Wing UAV”. Middle East Technical University, 2009.

[5] Renshan Zhang, Jiyang Zhang, and Huangchao Yu. “Review of modeling and control in UAV autonomous maneuvering flight”. In: *Proceedings of 2018 IEEE International Conference on Mechatronics and Automation* (2018).

[6] HaiYang Chao, YongCan Cao, and YangQuan Chen. “Autopilots for Small Unmanned Aerial Vehicles: A Survey”. In: *International Journal of Control, Automation, and Systems* 8.1 (2010), pp. 36–44.

[7] Y. Fan. “Autonomous and Intelligent Control of the Unmanned Aerial Vehicle”. In: *SCIENTIA SINICA Technologica* 47.3 (2017), pp. 221–229.

[8] Maziar Arjomandi. “Classification of Unmanned Aerial Vehicles”. In: *Mechanical Engineering 3016: Aeronautical Engineering* (2006).

[9] Hazim Shakhatreh et al. “Unmanned Aerial Vehicles (UAVs): A Survey on Civil Applications and Key Research Challenges”. In: *IEEE Access* (2019).

[10] Sonia Waharte and Niki Trigoni. “Supporting Search and Rescue Operations with UAVs”. In: *2010 International Conference on Emerging Security Technologies*. 2010.

[11] Yuntao Wang et al. “Lifesaving with RescueChain: Energy-Efficient and Partition-Tolerant Blockchain Based Secure Information Sharing for UAV-Aided Disaster Rescue”. In: *IEEE INFOCOM 2021 - IEEE Conference on Computer Communications*. May 2021.

[12] Dimosthenis C. Tsouros, Stamatia Bibi, and Panagiotis G. Sarigiannidis. “A Review on UAV-Based Applications for Precision Agriculture”. In: *MDPI Information* (Nov. 2019).

[13] Telmo Adão et al. “Hyperspectral Imaging: A Review on UAV-Based Sensors, Data Processing and Applications for Agriculture and Forestry”. In: *MDPI Remote Sensing* (2017).

[14] S. Khanal, J. Fulton, and S. Shearer. “An Overview of Current and Potential Applications of Thermal Remote Sensing in Precision Agriculture”. In: *Computers and Electronics in Agriculture* 139 (June 2017), pp. 22–32.

[15] III C. T. Howell et al. *The First Government Sanctioned Delivery of Medical Supplies by Remotely Controlled Unmanned Aerial System*. Tech. Rep. Hampton, VA, USA: NASA Langley Research Center, 2016.

[16] Y. Ham et al. “Visual Monitoring of Civil Infrastructure Systems via Camera-equipped Unmanned Aerial Vehicles (UAVs): A Review of Related Works”. In: *Visualization in Engineering* 4.1 (2016), p. 1.

[17] I. Sa and P. Corke. “Vertical Infrastructure Inspection using a Quadcopter and Shared Autonomy Control”. In: *Field and Service Robotics*. Berlin, Germany: Springer, 2014, pp. 219–232.

[18] Christian Gelzer. *X-45 Unmanned Combat Air Vehicle (UCAV)*. 2009. URL: https://www.nasa.gov/aeronautics/x-45/.

[19] *Predator RQ-1 / MQ-1 / MQ-9 Reaper UAV*. Accessed: January 28, 2024. 2022. URL: https://www.airforce-technology.com/projects/predator-uav/.

[20] Inside Unmanned Systems. *Delair Introduces the UX11 Ag UAS*. Accessed: January 28, 2024. Nov. 2018. URL: https://insideunmannedsystems.com/delair-introduces-the-ux11-ag-uas/.

[21] PX4 Development Team. *MRO Pixhawk*. May 2023. URL: https://docs.px4.io/v1.11/en/flight_controller/mro_pixhawk.html.

[22] Ryan Pickrell. *Nearly 100 countries have military drones, and it's changing the way the world prepares for war*. Sept. 2019. URL: https://www.cnas.org/press/in-the-news/nearly-100-countries-have-military-drones-and-its-changing-the-way-the-world-prepares-for-war.

[23] *Jouav - Emergency Response*. Accessed: January 28, 2024. URL: https://www.jouav.com/industry/emergency-response.

[24] *HAMMERHEAD – ELECTRIC VTOL FIXED WING UAV*. Accessed: January 28, 2024. URL: https://www.technosysind.com/hammerhead-electric-vtol-drone-uav/.

[25] A. Dharmawan et al. "The Obstacle Avoidance System In A Fixed-Wing UAV When Flying Low Using LQR Method". In: *2019 International Conference on Computer Engineering, Network, and Intelligent Multimedia (CENIM)*. Surabaya, Indonesia, 2019.

[26] S. Ayyildiz and H. Yazici. "Pitch Control by LQR for Fixed Wing Aircraft during Microburst Encounter". In: *5th International Conference on Advances in Mechanical Engineering*. Istanbul, 2019.

[27] P. Poksawat, L. Wang, and A. Mohamed. "Automatic tuning of attitude control system for fixed-wing unmanned aerial vehicles". In: *IET Control Theory Appl.* 10.17 (2016), pp. 2233–2242.

[28] Pakorn Poksawat, Liuping Wang, and Abdulghani Mohamed. “Gain Scheduled Attitude Control of Fixed-Wing UAV With Automatic Controller Tuning”. In: *IEEE Transactions on Control Systems Technology* 26.4 (July 2018).

[29] Mark C. Palframan, Kyle T. Guthrie, and Mazen Farhood. “An LPV Path-Following Controller for Small Fixed-Wing UAS”. In: *2015 IEEE 54th Annual Conference on Decision and Control (CDC)*. Osaka, Japan, Dec. 2015.

[30] Roger Wacker, Steve Munday, and Scott Merkle. “X-38 Application of Dynamic Inversion Flight Control”. In: *24th Annual AAS Guidance and Control Conference*. Jan. 2001.

[31] Su Cao et al. “Adaptive Incremental Nonlinear Dynamic Inversion Control Based on Neural Network for UAV Maneuver”. In: *Proceedings of the 2019 IEEE/ASME International Conference on Advanced Intelligent Mechatronics*. Hong Kong, China, July 2019.

[32] Yuri Shtessel et al. *Sliding Mode Control and Observation*. Birkhäuser, 2014.

[33] Changchun Bao et al. “Design of a Fixed-Wing UAV Controller Based on Adaptive Backstepping Sliding Mode Control Method”. In: *IEEE Access* (Dec. 2021).

[34] T. Espinoza et al. “Backstepping - Sliding Mode Controllers Applied to a Fixed-Wing UAV”. In: *Journal of Intelligent & Robotic Systems* (2014).

[35] Siri Mathisen et al. “Precision Deep-Stall Landing of Fixed-Wing UAVs using Nonlinear Model Predictive Control”. In: *Journal of Intelligent & Robotic Systems* (2021).

[36] Mina Kamel et al. “Model Predictive Control for Trajectory Tracking of Unmanned Aerial Vehicles Using Robot Operating System”. In: *Robot Operating System (ROS) The Complete Reference (Volume 2)*. Springer, 2017.

[37] Ruben Kleiven, Kristoffer Gryte, and Tor Arne Johansen. “Robust and Gain-Scheduled Flight Control of Fixed-Wing UAVs in Wind and Icing Conditions”. In: *2022 IEEE Aerospace Conference (AERO)*. 2022.

[38] Natassya B. F. Silva et al. “Dynamic Inversion and Gain-Scheduling Control for an Autonomous Aerial Vehicle with Multiple Flight Stages”. In: *Journal of Control, Automation and Electrical Systems* (2017).

[39] Zhijia Zhao, Xiuyu He, and Choon Ki Ahn. “Boundary Disturbance Observer-Based Control of a Vibrating Single-Link Flexible Manipulator”. In: *IEEE Transactions on Systems, Man, and Cybernetics: Systems* (2019).

[40] Wen-Hua Chen et al. “Disturbance-Observer-Based Control and Related Methods—An Overview”. In: *IEEE Transactions on Industrial Electronics* 63.2 (Feb. 2016).

[41] Shihua Li et al. *Disturbance Observer-Based Control: Methods and Applications*. CRC Press, 2014.

[42] Emre Sariyildiz, Roberto Oboe, and Kouhei Ohnishi. “Disturbance Observer-based Robust Control and Its Applications: 35th Anniversary Overview”. In: *IEEE Transactions on Industrial Electronics* (2019).

[43] Bayandy Sarsembayev, Kanat Suleimenov, and Ton Duc Do. “High Order Disturbance Observer Based PI-PI Control System With Tracking Anti-Windup Technique for Improvement of Transient Performance of PMSM”. In: *IEEE Access* (Apr. 2021).

[44] Umair Javaid et al. “High-Performance Adaptive Attitude Control of Spacecraft With Sliding Mode Disturbance Observer”. In: *IEEE Access* (Apr. 2022).

[45] Jun Yang et al. “Design of a Prediction-Accuracy-Enhanced Continuous-Time MPC for Disturbed Systems via a Disturbance Observer”. In: *IEEE Transactions on Industrial Electronics* 62.9 (Sept. 2015).

[46] Myunghwan Eom, Dongkyoung Chwa, and Dane Baang. “Robust Disturbance Observer-Based Feedback Linearization Control for a Research Reactor Considering a Power Change Rate Constraint”. In: *IEEE Transactions on Nuclear Science* (June 2015).

[47] Zhengguo Huang and Mou Chen. “Coordinated Disturbance Observer-Based Flight Control of Fixed-Wing UAV”. In: *IEEE Transactions on Circuits and Systems II: Express Briefs* 69.8 (Aug. 2022).

[48] Jean Smith, Cunjia Liu, and Wen-Hua Chen. “Disturbance Observer Based Control for Gust Alleviation of a Small Fixed-Wing UAS”. In: *2016 International Conference on Unmanned Aircraft Systems (ICUAS)*. 2016.

[49] Jun Yang et al. “Optimal Path Following for Small Fixed-Wing UAVs Under Wind Disturbances”. In: *IEEE Transactions on Control Systems Technology* (2021).

[50] Taha Hamid et al. “Pitch Attitude Control for an Aircraft using Linear Quadratic Integral Control Strategy”. In: *2019 22nd International Multitopic Conference (INMIC)*. 2019.

[51] Albert Farre Gabernet. “Controllers for Systems with Bounded Actuators: Modeling and control of an F-16 aircraft”. University of California, Irvine, 2007.

[52] *Airplane’s Body, Stability and Wind Axis*. Sept. 2011. URL: https://dodlithr.blogspot.com/2011/09/airplanes-stability-axis.html.

[53] Bernard Etkin. *Dynamics of Atmospheric Flight*. John Wiley & Sons, Inc., 1972.

[54] Luat T. Nguyen et al. *Simulator Study of Stall/Post-Stall Characteristics of a Fighter Airplane With Relaxed Longitudinal Static Stability*. Technical Paper 1538. NASA, 1979.

[55] B. Stevens and F.L. Lewis. *Aircraft Control and Simulation*. Wiley, 1992.

[56] *U.S. Military Specification MIL-F-8785C*. Nov. 1980.

[57] *Controller Diagrams*. Accessed: 9/28/2023. URL: https://docs.px4.io/main/en/flight_stack/controller_diagrams.html.

[58] Sridhar Seshagiri and Hassan K. Khalil. “Robust output feedback regulation of minimum-phase nonlinear systems using conditional integrators”. In: *Automatica* (2005).

[59] Ekprasit Promtun and Sridhar Seshagiri. “Sliding Mode Control of Pitch-Rate of an F-16 Aircraft”. In: *Proceedings of the 17th World Congress of The International Federation of Automatic Control*. Seoul, Korea, July 2008.

[60] C. Hancer et al. “Robust Position Control of a Tilt-Wing Quadrotor”. In: *49th IEEE Conference on Decision and Control*. Dec. 2010.